Harald Spreitzer, BSc

Structure and Morphology of Dioctyloxybenzothieno-benzothiophene Thin Films

MASTER'S THESIS

to achieve the university degree of
Diplom-Ingenieur

Master's degree programme of
Technical Physics

submitted to

GRAZ UNIVERSITY OF TECHNOLOGY

Supervisor
Ao.Univ.-Prof. Dipl.-Ing. Dr.techn. Roland Resel
Institute of Solid State Physics
Graz University of Technology

Graz, April 2016

AFFIDAVIT

I declare that I have authored this thesis independently, that I have not used other than the declared sources/resources, and that I have explicitly indicated all material which has been quoted either literally or by content from the sources used. The text document uploaded to TUGRAZonline is identical to the present master‘s thesis dissertation.

Date

Signature

Acknowledgement

First of all, special thanks to my supervisor Roland Resel for his great support and encouragement during my whole thesis. Being part of his working group and specially the opportunity to perform synchrotron measurements at BESSY in Berlin and Diamond in the United Kingdom were a great experience for me.
I would like to thank all my colleagues of our group Andrew Jones, Stefan Pachmajer, Magdalena Truger, Benedikt Schrode, Paul Christian, Katrin Unger Martin Tazreiter and Myles Rooney for inducting me patiently into the work in our laboratories and always taking the time to help me. Furthermore I wish to thank Benjamin Kaufmann and Christian Teichert at the Montan University in Leoben for the AFM measurements and analysis of my samples. I also would like to thank all members of the institute, especially Elisabeth Stern, Birgit Kunert and Harald Kerschbaumer for all their assistance.
Many thanks to my friends Markus Neuschitzer and Antonius Dorda for their big help and of course to my girlfriend Melanie Schriebl for encouraging me to resume my studies. Last, but by no means least, I would particularly like to thank my parents for all their support and love. Without you this wouldn't have been possible.

Abstract

The family of benzothieno[3,2-b]benzothiophene (BTBT) molecules currently holds the record of charge transport mobility within organic thin film transistors, which is more than 43 cm^2/Vs [1]. Therefore, the crystallization of this molecules within thin films is of large interest for the organic semiconductor reserch. The subject of this study was to study thin films in terms of morphology and crystallographic structure of the molecule dioctyloxy-BTBT starting from the sub-monolayer regime up to device relevant thicknesses. The thin films were prepared by physical vapour deposition under high vacuum of 10^{-7}mbar using a Knudsen cell. The crystallization of samples performed with a deposition rate of about 0.1nm/min and 1.0nm/min, unheated and to 75°C heated substrates were investigated. It was found that the already known surface induced phase of dioctyloxy-BTBT films is formed at the substrate surface as observed by grazing incidence X-ray diffraction studies. The combined study of X-ray reflectivity and atomic force microscopy shows a big effect of the deposition condition on the layer growth of sub-monolayers and a pronounced layer by-layer growth was found. For the XRR fitting two different software packages are used, *Stochfit* for sub-monolayer and a few monolayer samples and *X'Pert Reflectivity* suitable for multilayers. This integral information could be correlated to the local information of the AFM via the coverage. Outstandingly the closing of the layer could be observed up to large film thicknesses, a surface roughness of 3 partial layers is continuously observed starting from the first few monolayers up to thick films of 32 monolayers.

Kurzfassung

Die Familie der Benzothieno[3,2-b]benzothiophene (BTBT) Moleküle hält zurzeit den Rekort für Ladungsträgermobilität mit 43 cm^2/Vs der organischen Dünnschichttransitoren [1]. Daher ist die Kristallstruktur dieser Moleküle für dünne Schichten besonders interesant für die organische Halbleiterforschung. Inhalt dieser Arbeit ist die Untersuchung der Morphologie und kristallographischer Struktur von Dioctyloxy-BTBT Molekülen vom submonolagen Bereich bis hin zu Bauteil relevanten Probendicken. Die Dünnschichtproben wurden durch Aufdampfen im Hochvakuum bei einem Druck von 10^{-7}mbar unter Verwendung einer Knudsenzelle hergestellt. Dabei wurde die Kristallisation bei niedriger Aufdampfrate von 0.1nm/min bei ungeheiztem und mit 75°C geheiztem Substrat, als auch bei hoher Aufdampfrate von 1.0nm/min untersucht. Es wird gezeigt, dass sich die bereits in Filmen durch Spin-Coaten geformte, bekannte oberflächeninduzierte Phase bildet, durch Kleinwinkelstreumessungen. Untersuchung durch Röntgenreflektivität und AFM-Bilder zeigen ein deutliches Lage für Lage Wachstum. Besonders für das Wachstum der Submonolage spielen die unterschiedlichen Aufdampfbedingungen eine große Rolle. Das Fitten der Röntgenreflektivitätmessungen erfolgt durch zwei Programme, *Stochfit* für Submonolagen und dünnen Schichten mit wenigen Monolagen und *X'Pert Reflectivity* geeignet für Mehrlagenfilme. Die aus diesen Fits berechnete Schichtbedeckung konnte mit den AFM Messungen verglichen werden. Untersuchungen zeigen ein füllen der Lagen bis hin zu dickeren Filmen von 32 Monolagen mit einer konstant bleibenden Oberflächenrauhigkeit von drei Monolagen.

Contents

1 Introduction

1.1 Crystallization of Molecules at Surfaces

Molecular packing is important for charge transport capability, so it is important to understand and control them. This makes molecular packing a key aspect in the field of organic electronics for optimal design of organic field effect transistors (OFETs) [2–5]. Since charge transport occurs only within the first few molecular layers, the molecular packing at the substrate-film interface is of great importance for device optimization [6]. The prototypical organic semiconductor pentacene was the first material which demonstrated, that structures close to the substrate are not always the same as those in the bulk [7,8]. These observed polymorphic phases are so called thin film, or substrate induced phases (SIPs) [7,8] and have since been found in other systems [9,10]. The rod-shapes in figure 1.1 symbolize the molecules, just to give an idea of the difference between the single crystal structure of the bulk, where close packing is accepted to be the main driver, and SIPs which are found to be less dense than the bulk structure. [11] Usually they are less energetically favorable and far off the thermodynamic equilibrium making them metastable. They are stabilized close to the substrate because of improved compatibility of the structure with the flat surface of the substrate [12,13]. Still, the fact that SIPs often slowly convert to the single crystal structure over time or with annealing may suggest that SIPs are mainly a metastabile form induced by the substrate [14]. The π -conjugated molecules show most often a small change in the tilt angle between SIPs and bulk phases of the approximately upright standing molecules and the substrate. This leads to enhanced molecule-substrate and molecule-molecule interactions and a decrease in the out-of-plane lattice spacing such that the two phases are similar but distinct from one another [15, 16]. Beside the

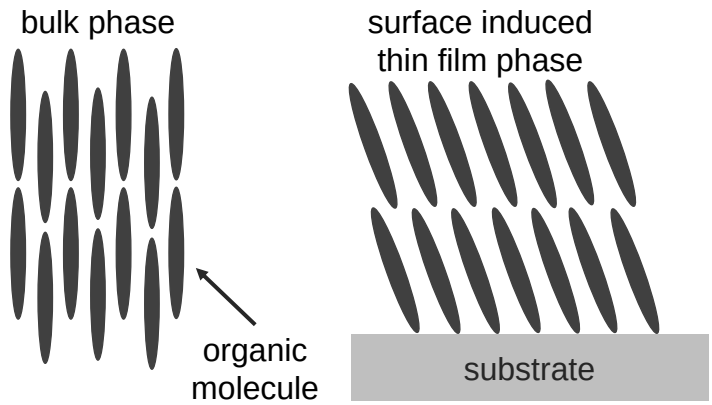

Figure 1.1: Schematic drawing of the single crystal bulk phase (left) and a surface induced phase (right) [17]

substrate also the preparation conditions have an influence of the film structure. For spin coated films the solvent with its evaporation rate may have an impact on the crystallization speed allowing a more, or less metastable formation [17]. In case of physical vapour deposition providing conditions far of the thermodynamical equilibrium, crystallization controlled via the deposition rate can have an influence on the crystal structure, as well as the diffusion process on the substrate dependent on the substrate temperature or preparation like sputtering. However, after a certain film thickness bulk structure can start to grow on top so often these two phases coexist within a thick film [10, 16]. The structure of the SIP therefor may influence charge mobility and potential device performance when present due to its proximity to the substrate.

1.2 The Molecule C_8BTBT

Dioctyloxy[1]benzothieno[3,2-b]benzothiophene (in short C_8O-BTBT-OC_8 or oBTBT) is part of the family of BTBT molecules which currently hold the record of charge transport mobility within organic thin film transistors, which is more than 40.3 cm^2/Vs [18]. Therefore, the crystallization of this molecules within thin films is of large interest for the organic semiconductor industry. They are easy to handle because of their good air stability [19, 20]. Like C_8O-BTBT-OC_8 (figure 1.2) all molecules of these family consist of

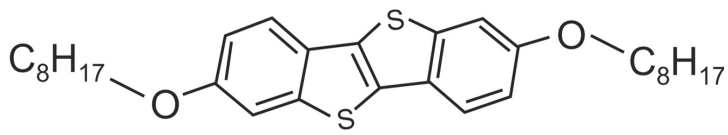

Figure 1.2: Chemical structure of Dioctyloxy[1]Benzothieno[3,2-b]benzothiophene

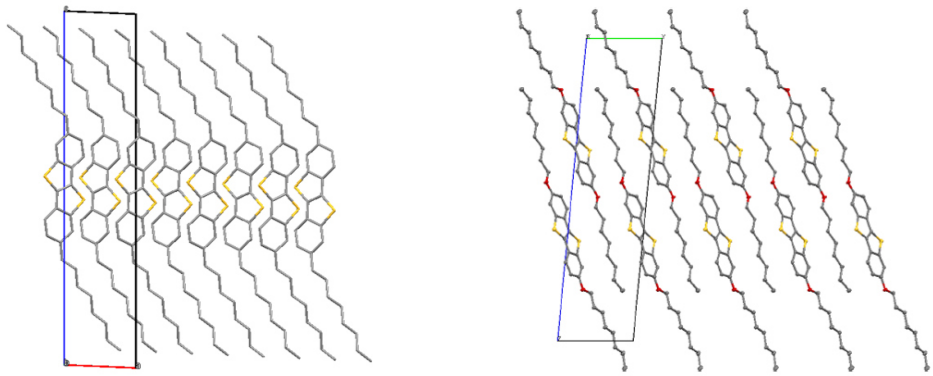

(a) (b)

Figure 1.3: Crystal bulk structure of (a) C_8-BTBT-C_8 and (b) C_8O-BTBT-OC_8 with oxygen an atoms between core and alkylchain [14] (the hydrogen atoms have been removed for clarity)

three parts: The aromatic core as a conjugated system, providing semiconducting properties and the two attached alkyl side chains for solution processing. There are plenty of variations of the sidechain length all resulting in about the same molecular packing of bulk structure (figure 1.3 left), and no SIP with herringbone configuration was present so far. However, a big change in the type of packing appears when an oxygen atom is added between the sidechains and the core. A single bulk polymorph with π - π stacked, interdigitated molecules (figure 1.3 right) and also molecules aligned in a SIP of herringbone structure is found in thin films similar to the structure in figure 1.3 left. The SIP is known to be produced from spin coated and thin dropcasted film, whereas bulk phase appears in thicker

Table 1.1: Unit-cell parameters and electron density ρ_e of different Phases of C_8O-BTBT-OC_8 Films [14]

	a [Å]	b [Å]	c [Å]	α [deg]	β [deg]	γ [deg]	ρ_e[nm^{-3}]
SIP	6.02	7.75	31.08	90.00	97.00	90.00	373
Bulk	5.52	8.07	31.06	94.48	92.99	105.70	405

dropcasted films [14]. The unit-cell of these different crystal phases is shown in Table 1.1.
One sees the bulk structure has a clearly higher electron density due to closer packing. The SIP unit-cell is monoclinic and both structures contain two molecules in the unit.
X-ray measurements suggest that the BTBT cores are aligned approximately parallel to the a-axis in the 020 plane and the alkyl chains are bending away from the cores toward the substrate [14]. A measurement after 6 month showed a slight conversion of the SIP to the bulk structure over time but so far it is not clear wether this would continue till only bulk phase is present. Solvent vapor annealing significantly increases this conversion rate.

1.3 Crystallography of Low Symmetry Systems

An ideal crystal consists of an infinite repetition of identical building blocks, which are atoms or groups of atoms, apart from imperfections and impurities that may be accidentally included [21]. This block is called the basis. The periodic arrangement can be described by a translation using a three dimensional lattice. Every point in the three dimensional lattice can be reached by a crystal translation T with the translations vectors **a**, **b**, **c** and the integers u_1,u_2 and u_3.

$$\mathbf{T} = u_1\mathbf{a} + u_2\mathbf{b} + u_3\mathbf{c} \tag{1.1}$$

The lattice also can be defined by the unit-cell with the parameters $a = |\mathbf{a}|$,

Table 1.2: Two cases of crystal systems most for molecular crystals with their interplanar spacing d_{hkl} [22]

Crystal system	Constraints	$1/d^2_{hkl}$
Monolinic	$a \neq b \neq c$ $\alpha = \beta = 90° \neq \gamma$	$\frac{h^2}{a^2 \sin^2 \beta} + \frac{k^2}{b^2} + \frac{l^2}{c^2 \sin^2 \beta} + \frac{2hl \cos \beta}{ac \sin^2 \beta}$
Triclinic	$a \neq b \neq c$ $\alpha \neq \beta \neq \gamma$	Equation 1.3

$b = |\mathbf{b}|$, $c = |\mathbf{c}|$ and the angles $\alpha = \angle(\mathbf{b}, \mathbf{c})$, $\beta = \angle(\mathbf{a}, \mathbf{c})$, $\gamma = \angle(\mathbf{a}, \mathbf{b})$.. There are 14 different lattice types in three dimension. The general case is triclinic shown in table 1.2.
The volume of this crystallographic unit-cell can be calculated with

$$V = abc\sqrt{1 - \cos^2 \alpha - \cos^2 \beta - \cos^2 \gamma + 2 \cos \alpha \cos \beta \cos \gamma} \tag{1.2}$$

The interplanar spacing d_{hkl} follows the formula

$$\begin{aligned} \frac{1}{d^2_{hkl}} =& \frac{1}{V^2}(b^2c^2h^2 \sin^2 \alpha + a^2c^2k^2 \sin^2 \beta + 2hkabc^2(\cos \alpha \cos \beta - \cos \gamma) \\ &+ 2kla^2bc(\cos \beta \cos \gamma - \cos \alpha) + 2hlab^2c(\cos \gamma \cos \alpha - \cos \beta) \\ &+ a^2b^2l^2 \sin^2 \gamma) \end{aligned} \tag{1.3}$$

To get the possible X-ray reflection one needs to consider the Fourier analysis to describe the periodic electron number density $n(\mathbf{r})$.

$$n(\mathbf{r}) = \sum_{\mathbf{G}} n_{\mathbf{G}} \, e^{i\mathbf{G}\mathbf{r}} \tag{1.4}$$

It is invariant to translations $n(\mathbf{r}+\mathbf{T})=n(\mathbf{r})$. The reciprocal lattice vectors $\mathbf{G}$ which will later be used to describe the Laue conduction has to be found. It is mapped by a set of axis reciprocal lattice vectors $\mathbf{a}^*$, $\mathbf{b}^*$ and $\mathbf{c}^*$

$$\mathbf{G} = h\mathbf{a}^* + k\mathbf{b}^* + l\mathbf{c}^* \tag{1.5}$$

Again h,k and l are integers. The axis vectors can be constructed via the

primitive vectors of the crystal lattice

$$\mathbf{a}^* = 2\pi \frac{\mathbf{b} \times \mathbf{c}}{\mathbf{a} \cdot \mathbf{b} \times \mathbf{c}} \qquad \mathbf{b}^* = 2\pi \frac{\mathbf{c} \times \mathbf{a}}{\mathbf{a} \cdot \mathbf{b} \times \mathbf{c}} \qquad \mathbf{c}^* = 2\pi \frac{\mathbf{a} \times \mathbf{b}}{\mathbf{a} \cdot \mathbf{b} \times \mathbf{c}} \tag{1.6}$$

The Miller indices (hkl), which determine planes in a crystal at certain intercepts on the axis in terms of the lattice constants a, b, c are found by taking the reciprocal values and using the smallest integers with the same ratio.

2 Experimental Techniques

2.1 X-ray Diffraction

When electromagnetic radiation impinges on a periodic structure with length scale of the wavelength (for X-rays with energy of 3 to 8keV this corresponds to a wavelength of 0.15 to 0.4nm) diffraction effects are observed with phenomena like constructive and destructive interference [22].
The scattering process of x-rays used for structural investigation is called Thomson scattering. The X-rays are scattered elastically by electrons, making them oscillate like a dipole with the frequency of the incoming beam, so the electron becomes a source of dipole radiation. Since it is elastic the wavelength of the X-rays is conserved for incoming and outgoing radiation. The condition of interference can be obtained geometrically, visualized in figure 2.1 and is called the Bragg equation.

$$n\lambda = 2d_{hkl} \sin\left(\frac{2\theta}{2}\right) \tag{2.1}$$

The interplanar spacing d_{hkl} specified by the Miller indices and unit cell parameter is given in table 1.2 for different crystal systems. The maximum

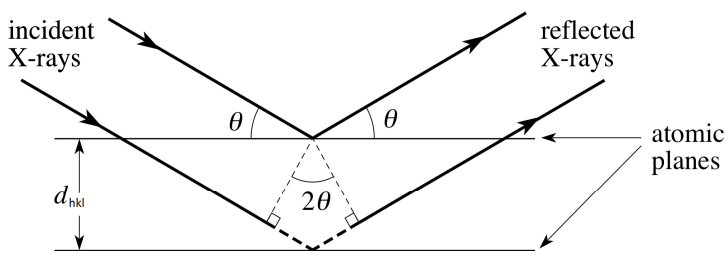

Figure 2.1: Illustration of Braggs law [23]

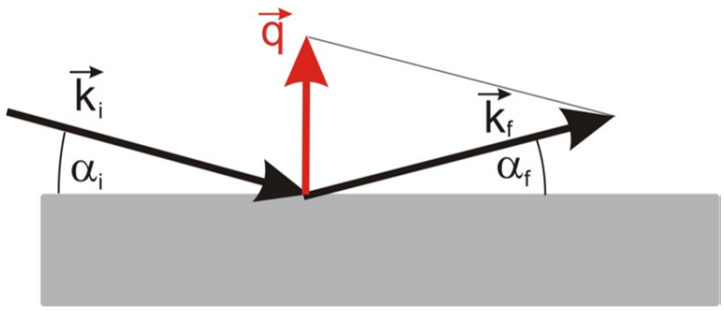

Figure 2.2: Geometrical subtraction of the primary beam $\mathbf{k}_0$ and the scattered beam $\mathbf{k}$ [24]. In specular condition α_i=α_f

of the scattered intensity is only observed, when the path difference is a multiple n of the wavelength λ. This equation 2.1 was applied in 1913 by W.H. Bragg and W.L.Bragg for positioning x-ray scattering peaks in angular space. Another way to describe the relation between lattice vectors **G** and scattering vector **q** is the Laue condition. To calculate the vector **q** one has to subtracted the incoming wavevector $\mathbf{k}_0$ and the outgoing wavevector **k** shown in figure 2.2 [21] and equation 2.2.

$$\mathbf{k}_f - \mathbf{k}_i = \mathbf{q} \tag{2.2}$$

The scattering vector **q** then points normal to the crystallographic plane (hkl) and has a length of $|q| = 4\pi/\lambda * sin(\theta)$. The reciprocal lattice vector G is given by the Miller indices and the primitive vectors **a***, **b*** and **c***. **G** and **q** are pointing in the same direction so the Laue condition then follows

$$\mathbf{q} = \mathbf{G} \tag{2.3}$$

In this thesis all diffraction plots are using the scattering vector q, so they are independent on the wavelength

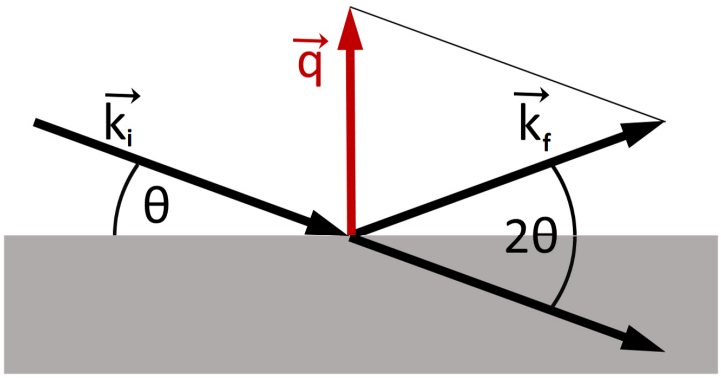

Figure 2.3: Schematic drawing of a θ/θ measurement [17]

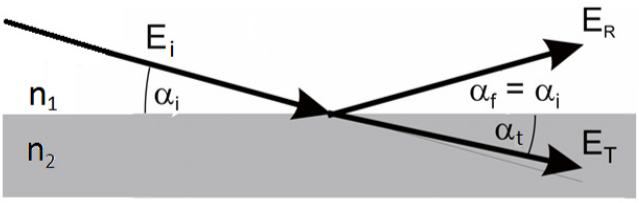

Figure 2.4: Electrical field vectors **E** of an incoming beam, which partly gets reflected and transmitted at the surface [24]

2.2 X-ray Reflectivity (XRR)

X-Ray reflectivity considers the optical reflection and is measured in specular condition, so the primary incoming beam and the outgoing beam is the same angle $\alpha_i = \alpha_f$. In a θ/θ scan the sample stage stays at the same position while measuring, whereas the incidence beam varies by rather small angles and the detector gets positioned at 2 θ measuring the diffracted intensity (figure 2.3). In this thesis measurements with θ = 0.05-4.5° are performed. The primary beam has to be in a parallel configuration, having a divergence of less 0.05°, so it is highly collimated [22]. Depending on the refractive index of the medias, optical reflection and transmission occurs (figure 2.4).

The complex refractive index for X-rays are given by

$$\begin{aligned} n &= 1 - \delta - i\beta \\ \delta &= \frac{\lambda^2}{2\pi} r_\mathrm{e} \rho_\mathrm{e} \\ \beta &= \frac{\lambda}{4\pi} \mu \end{aligned} \tag{2.4}$$

with the classical electron radius r_e=2.82 x 10^{-6}nm, the X-ray wavelength λ, the attenuation coefficient μ and the electron density ρ_e. According to Snell's law of refraction the refractive indices of the incoming media n_1 and transmitted media n_2 are in relation to the cosine of the two angles

$$\frac{n_1}{n_2} = \frac{\cos \alpha_t}{\cos \alpha_i} \tag{2.5}$$

When absorption is negligible ($\beta \approx 0$) and with the simplification n_1=1, the condition of total reflection ($\alpha_t = 0$) is fulfilled below a critical angle α_c.

$$\alpha_c = \sqrt{2\delta} \tag{2.6}$$

Since this angle is depending on the electron density it gives important information about the specimen material Again the oscillations of the X-ray intensity caused by the interference involving the sample surface are called Kiessig fringes. Depending on the surface roughness, film thickness, interface roughness and electron density the shape of these fringes varies as shown in figure 2.5.

2.3 PANalytical Empyrean

The samples are measured with a PANalytical Empyrean diffractometer having an experimental setup given in figure 2.6. On the left side is the water cooled copper tube powered with 40kV and 40mA.After the beam passes a divergence slit of 1/32° and a 4mm mask, adjusting it to sample size, a parallel beam mirror collimates the X-rays to a parallel beam with a divergence of only 0.055°mainly providing CuKα radiation of $\lambda = 0.154$nm.

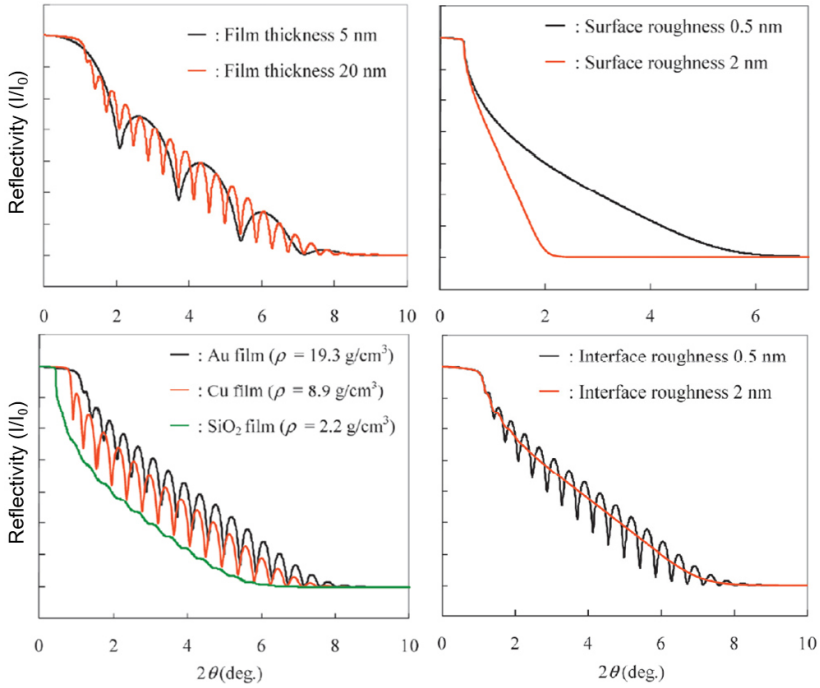

Figure 2.5: The influence of sample properties on the shape of the Kiessig fringes [25]

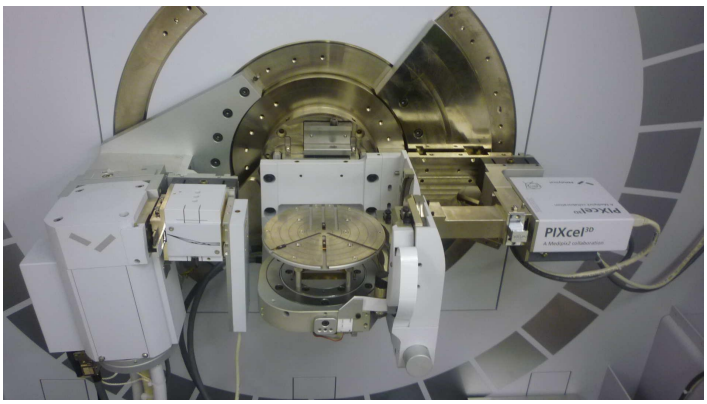

Figure 2.6: Setup of the PANalytical Empyrean for a XRR measurement [17]

Since in XRR only small angles are investigated a beam attenuator reduces the high radiation intensity, to protect the detector via a 0.125mm Ni-plate. The reduced intensity is corrected automatically in the plots. The moveable sample stage in the middle can be tilted, rotated and moved in height. The diffracted beam side consist of a 0.1mm anti-scatter slit and a 0.02rad Soller

slit, to reduce background and a solid state detector. This PIXcel^{3D} detector with 255x255 Pixel channels each of a size 55x55 μm.operates in a receiving slit mode 0D with three open channels for XRR where it acts like a point detector. The measurements are performed with a step size of 0.01° and a time of 8sec per step.

2.4 Fitting of a XRR Measurement

2.4.1 Parratt Formalism

The software for fitting the XRR measurements, *Stochfit* and *PANalytical X'pert Reflectivity* both are using the Parratt formalism [26]. It uses a recursions formula to calculate the total reflectivity amplitude, which gives information about layer thickness refraction indices and with modification also about the surface and interface roughness. The dynamical scattering theory says that an electromagnetic wave $\mathbf{E}_i(\mathbf{r}) = \mathbf{E}_0(\exp i\mathbf{k}_i\mathbf{r})$ splits into a reflected and transmitted wave, $\mathbf{E}_r(\mathbf{r})$ and $\mathbf{E}_t(\mathbf{r})$ (figure 2.4)

$$\begin{aligned} \mathbf{E}_r(\mathbf{r}) &= r_s\mathbf{E}_i(\mathbf{r})\exp[i(\mathbf{k}_f - \mathbf{k}_i)r] \\ \mathbf{E}_t(\mathbf{r}) &= t_s\mathbf{E}_i(\mathbf{r})\exp[i(\mathbf{k}_t - \mathbf{k}_i)r] \end{aligned} \tag{2.7}$$

when it hits a surface. Here $\mathbf{q} = \mathbf{k}_f - \mathbf{k}_i$ is the wave vector transfer and r_s and t_s are the reflection and transmission coefficient calculated via the Fresnel equations [27]

$$r_s = \frac{k_{i,z} - k_{t,z}}{k_{i,z} + k_{t,z}}, t_s = \frac{2k_{i,z}}{k_{i,z} + k_{t,z}} \tag{2.8}$$

where the z-components of the incoming and transmitted wave $k_{i,z} = k\sin\alpha_i$ and $k_{t,z} = k\sin\alpha_t = k\sqrt{n^2 - \cos^2\alpha_i}$. Since n is about one for X-rays both cases, s- and p- polarization are effectively identical, so here only s-polarization is used. The Fresnel reflectivity which is the intensity of the Beam can be calculated via the reflection coefficient

$$r_F(q_z) = |r_s|^2 \approx \left(\frac{q_c}{2q_z}\right)^4 \tag{2.9}$$

for $q_z \gg q_c$. The z-component of the wave vector reads $q_z = 2k\sin(\alpha_i)$ and the critical wave vector $q_c = 2k\sin(\alpha_c)$ is a function of the critical angle α_c. Parratt developed a recursive formalism that provides the reflectance R_j at the interface between the layer j and j+1

$$R_j = \frac{R_{j+1}\exp(-iq_{z,j+1}\Delta z_{j+1}) + r_{j,j+1}}{R_{j+1}r_{j,j+1}\exp(-iq_{z,j+1}\Delta z_{j+1}) + 1} \tag{2.10}$$

The Fresnel reflection coefficient here is given by

$$r_{j,j+1} = \frac{k_{z,j} - k_{z,j+1}}{k_{z,j} + k_{z,j+1}} \tag{2.11}$$

with

$$k_{z,j} = k\sqrt{n_j^2 - \cos^2\alpha_i}, \tag{2.12}$$

the z-componet of the vector in layer j with the refration index $n_j = 1-\delta_j - i\beta_i$ and the layer thickness Δz_j. The wave vector $q_{z,j} = 2k_{z,j}$ is the transfer in the layer j. Starting with equation 2.8 and 2.10 the recursion can be carried out over all R_j can be summed over all N layers leading to the reflectance at the surface, approximately given by

$$R_0 \approx \sum_{j=1}^{N+1} r_{j,j+1}\exp\left(i\sum_{l=1}^{j-1} q_{z,l}\Delta z_l\right). \tag{2.13}$$

The total measurable reflectivity [28] is then

$$r = |R_0^2|. \tag{2.14}$$

With the continuous limit $N \to \infty$ and $\Delta z_l \to 0$ the kinematical approximated reflectance of the entire sample in eq. 2.13 far of the total reflection $q_z \gg q_c$ is given by

$$R(q_z) = \frac{4\pi}{q_z^2}\int_{-\infty}^{+\infty}\frac{d\rho(z)}{dz}\exp(iq_z z)dz \tag{2.15}$$

This means that density profile $\rho(z)$ and reflectance are connected via the Fourier transformation. Replacing the factor $1/q_z^2$ now with some Fresnel reflection, the reflectivity $r(q_z) = |R(q_z)|^2$ can be written as

$$r(q_z) = r_F(q_z)|F(q_z)|^2 \tag{2.16}$$

with the Fresnel reflectivity in eq. 2.9 The density profile of N layers with a gaussian roughness σ_n and $\Delta\rho_n = \rho_{n-1} - \rho_n$ has a form of

$$\rho(z) = \sum_{n=0}^{N} \Delta\rho_n erf\left(-\frac{z - z_n}{\sqrt{2}\sigma_n}\right) \tag{2.17}$$

with the Gaussian error function $erf(z) = \int_0^z \exp(-\zeta^2)d\zeta$, the complex structure factor is given by

$$F(q_z) = \sum_{n=0}^{N} \frac{\Delta\rho_n}{\rho_\infty} \exp(iq_z z_n) \exp(-\frac{q_z^2\sigma_n^2}{2}) \tag{2.18}$$

Where $\rho_\infty = \sum_n \Delta\rho_n$

2.4.2 Model-Independent Fitting

Here an electron density profile search is performed by a selected number of boxes N_B with a fixed thickness B_t, a smoothing parameter σ and a refractive index n_j for each box. Typically, the box thickness is in the order of 0.5Å [28]. Considering the environment (the so called "superphase") of the sample with the refraction index $n_0 = 1 - \delta_0 - i\beta$ the normal component of the wave vector $k_{z,j}$ in eq. 2.12 is constituted by

$$k_{z,j} = k[\sin^2(\alpha_i) - 2(n_0 - n_j)]^{1/2} \tag{2.19}$$

The refractive index of each box can be calculated by

$$\delta(z) = \delta_0 + \sum_{n=0}^{N_B} \left(\frac{\delta_{k+1} - \delta_k}{2}\right) \left[1 + erf\left(\frac{z - nB_t}{\sqrt{2}\sigma}\right)\right] \tag{2.20}$$

and for absorping films

$$\begin{aligned}\beta(z) =& \beta_0 + \left(\frac{\beta_a\delta_1/\delta_{N_B+1} - \beta_0}{2}\right)\left[1 + erf\left(\frac{z}{\sqrt{2}\sigma}\right)\right] \\ &+ \sum_{n=1}^{N_B-1} \frac{\beta_a}{\delta_{N_B+1}}\left(\frac{\delta_{n+1} - \delta_n}{2}\right)\left[1 + erf\left(\frac{z - nB_t}{\sqrt{2}\sigma}\right)\right] \\ &+ \left(\frac{\beta_{sub} - \beta_a\delta_{N_B}/\delta_{N_B+1}}{2}\right)\left[1 + erf\left(\frac{z - N_B B_t}{\sqrt{2}\sigma}\right)\right]\end{aligned} \tag{2.21}$$

where β_a is a variable parameter and β_{sub} is the absorbance of the substrate. There are two algorithm for minimization. One is a "greedy" search program which tests via a fitness function whether the calculated reflectivity R_{calc} is acceptable.

$$F = \sum_{i=1}^{N} [\ln(R_{calc}) - ln(R_{exp})]^{1/2} \tag{2.22}$$

R_{exp} is the measured reflectivity. Please note that R_{exp} does not consider the statistical errors, but since they are small with respect to the measured reflectivity a correction is generally not necessary. The other method is the simulated annealing. There the current state is accepted with the Boltzmann criteria over the previous state so it strongly depends on the initial temperature and the cooling schedule. This locates the global minimum of the fitness function Both methods are stochastic so there is no particular end for the search.

2.4.3 Software Comparison

The program *Stochfit* provides a bridge between model dependent and independent fit of the electron density but in this work only the model independent fit was used.
As mentioned before the entered film thickness had to be estimated and was divided into a defined number of equal boxes, varying only the electron densities in every box. So it has the advantage, that one has to know little information about the sample.. In this work, it was used from sub-monolayers up to films with an nominal thickness of 5 molecule layers. Thicker films

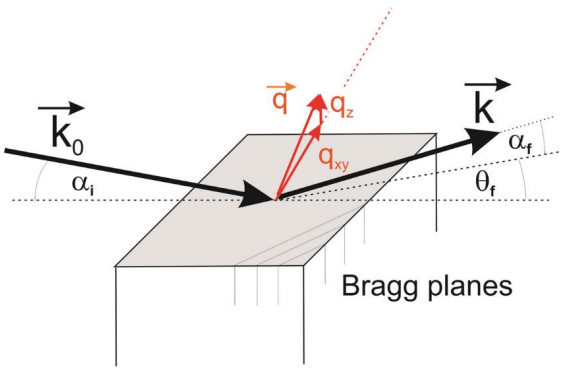

Figure 2.7: Schematic drawing of a grazing incident diffraction measurement of incident beam $\mathbf{k}_0$ and the scattered outgoing beam $\mathbf{k}$ [24]

couldn't be successfully fitted.

For the *PANalytical X'pert reflectivity* software a certain layer model has to be specified for the fit, with a chosen parameter frame of layer thicknesses, density and roughness. That of course means it is necessary to know several information before the start, which makes the fit more complicated, but in return delivers much more structural parameters for each layer. This software works better for thicker multilayer films.

2.5 Grazing Incident Diffraction (GIXD)

GIXD is a surface sensitivity method, to determine in-plane structures. When the incoming beam is kept at very small angles close to the critical angle a diffraction pattern is recorded by continuously increasing the scattering angle 2θ, while measuring the outgoing X-rays [22]. This schematic configuration is shown in figure 2.7. The momentum transfer $\mathbf{q}$ in which direction diffraction is probed, is almost perpendicular to the surface, so interplanar spacing of vertically inclined lattice planes are investigated. The created evanescent surface wave decays exponentially perpendicular to the surface, so only the first few nanometers may be elucidated. In the plot you can see the two components of the scattering vector, in-plane

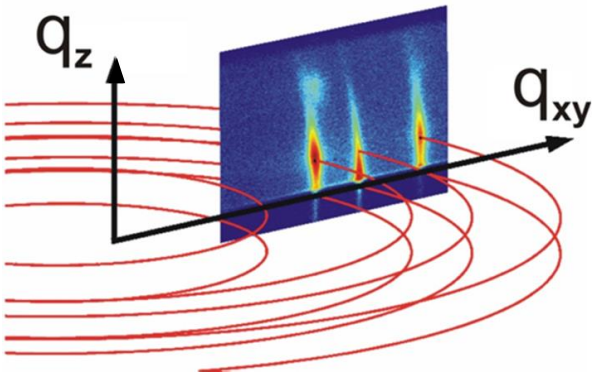

Figure 2.8: Measurement of a cross section in reciprocal space [24]

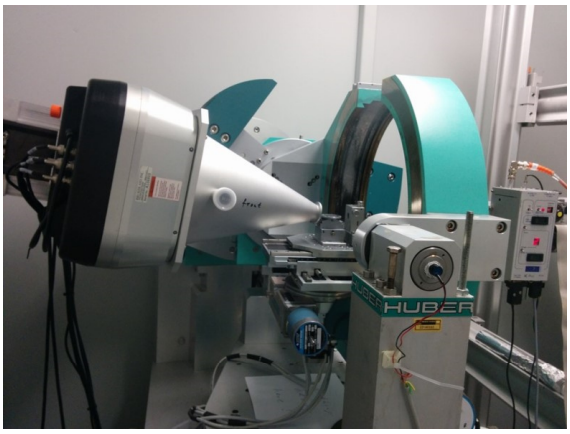

Figure 2.9: Experimental setup of the BESSY II beamline KMC-2 at Berlin [29]

$$q_{xy} = \sqrt{q_x^2 + q_y^2} \tag{2.23}$$

and perpendicular to the surface q_z [17].
The observed peaks are indexed by the in-house software PyGid via trial and error, to determine the unit cell. GIXD was performed at the BESSY II synchrotron in Berlin. The experimental setup of the beamline KMC-2 is shown in figure 2.9. The beam with a wave length of $\lambda = 1.00\AA$ and a shape of 1000μm x 50μm hit the sample on a movable stage at an angle of about 0.13°. A cross-wire 2D-detector (Bruker), protected by a cone to reduce the background, measured the scattered beam.

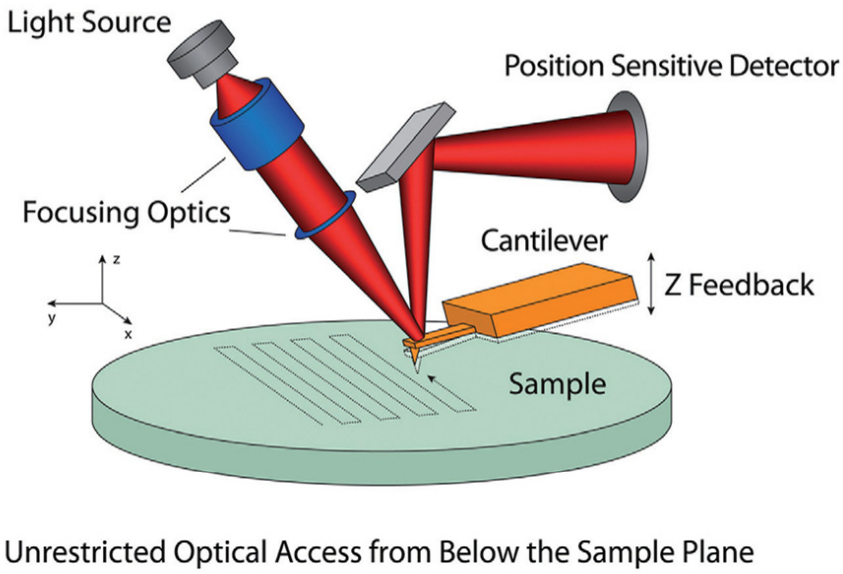

Figure 2.10: Schematic drawing of an optical lever detection system used in AFMs. The reflected light of the cantilever is read on a detector, raster scanning the sample [30]

2.6 Atomic Force Microscopy (AFM)

Atomic force microscopy has the ability to measure high-resolution topographical images, forces and/or elasticity of a specimen [30].
Starting in the late 1980s, when the first commercial AFM has been produced it nowadays delivers measurements at multiple special scales starting from a few nm up to some 100 microns in XY direction and a resolution in height of only an Angström. The micro fabricated cantilever physically interacts with the surface to scan, via a sharp tip. An optical tracking system measures the deflection or oscillation amplitude. It usually consists of a photo diode to detect the reflection of the laser on the tip. Another option is a super-luminescent diode off the back of the cantilever. The deflection or oscillations in height are done by a feedback-controlled piezo. Due to hysteresis, creep, aging and other non-linearity effects of the piezo the values have to be corrected via incorporated sensors. The limit of the resolution in XY is given by the size of the tip. In height the resolution

is limited by electronic and thermal noise, so again, it is in the order of an Angström. Advanced AFMs provide nanoscale images, simultaneously measuring electrical properties correlated with topography. This is especially interesting for organic semiconductors and photovoltaic materials, to characterize properties including bias, charge and current flow. In this work the data analysis and visualization were performed by the software package Gwyddion [31].

3 Sample Preparation

3.1 Substrate

In this thesis silicon wafers with 150nm thermally grown $Si0_2$ on it were used as substrates in the size of 1x1cm. This thin slice of semiconducting material is very common and widely used in electronic high-tech industries, including fabrication of integrated circuits and other micro-devices.
At first they were cleaned using a tissue with acetone on it. For the next step the substrates were put into an acetone sonic bath for 15min. Both procedures were repeated using 2-propanol. When the wafers were taken out of the sonic bath compressed CO_2 was used to dry them.
Lastly the substrates were loaded into to the ultra high vacuum (UHV) chamber, to sputter them with argon ions for 10min at a pressure of $5x10^{-5}$mbar and an ion current of 30mA.

3.2 Physical Vapor Deposition

For PVD one has to provide high vacuum and a thermal evaporate a source. The chamber used in this work is schematically drawn in figure 3.1. A rotary pump and two turbo molecular pumps supplied the system with a vacuum of approximately 10^{-7}mbar. The substrate was fixed on a heatable sample mounting equipped with a thermocouple to measure the temperature. A Knudsen cell, filled with the powder for the deposition, was heated by a filament. Monitored by a thermocouple at the bottom. To start and stop the deposition a shutter was moved. Via the frequency shift of a quartz microbalance the film thickness was calculated. The decreasing of the frequency due to the amount of deposited material is assumed to be linear, which is a good approximation.

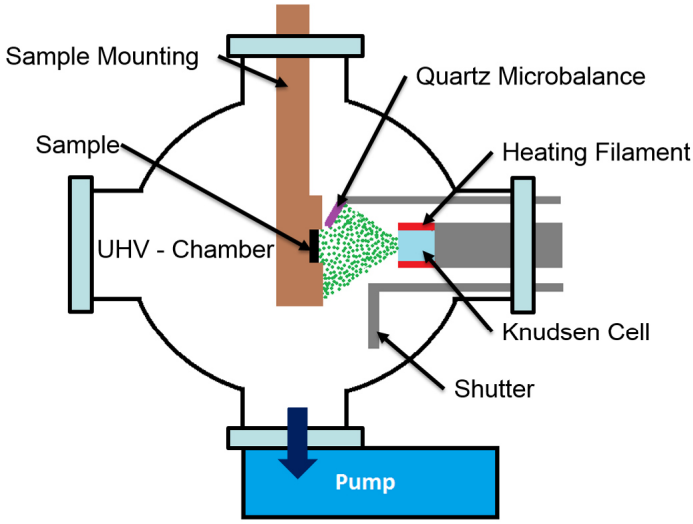

Figure 3.1: Schematic drawing of the ultra high vacuum chamber with a pressure of about 10^{-7}mbar, used for physical vapor deposition in this work

3.3 Sample Overview

Four series of samples with different deposition and preparation conditions were prepared shown in table 3.1. The first one had a rather low deposition rate and the substrate was kept at room temperature (RT). The second series, with approximately the same deposition rate, was heated during deposition. For one sub-monolayer sample the sputtering step was skipped, to see if this has an effect on the first monolayer, it was prepared with the same deposition conditions as the first series. The fourth and last series, with the substrate also kept at room temperature, was produced with a ten times higher deposition rate. Except the unsputtered sample, sub-monolayers and multilayers were prepared for all series.

Table 3.1: Overview of the prepared samples with the different deposition conditions, analyzed in the chapter results
Δf [Hz] ... Frequency change of the quartz micro balance
d_n [nm] ... nominal thickness calculated with equation 4.3
P [10^{-7}mbar] ... pressure during deposition
T [°] ... substrate temperature while deposition
r [Å/min] ... deposition rate

Series	Δf[Hz]	d_n[nm]	P[10^{-7}mbar]	T[°]	r [Å/min]
low deposition rate	35	1.2	2.8	RT	0.8
	50	1.7	3.6	RT	1.2
	75	2.5	5.3	RT	1.2
	100	3.3	1.2	RT	1.2
	150	5.0	1.2	RT	1.2
	400	13.2	6.0	RT	1.0
	3000	99.0	0.3	RT	1.2
heated substrates	25	0.8	3.2	73	1.0
	50	1.7	4.0	74	1.2
	75	2.5	3.7	75	1.1
	100	3.3	3.0	76	1.2
	150	5.0	4.8	75	1.2
	400	13.2	8.6	77	2.1
	3000	99.0	5.3	73	1.1
unsputtered	50	1.7	0.5	RT	1.2
high deposition rate	50	1.7	1.5	RT	9.9
	400	13.2	5.6	RT	9.9
	3000	99.0	4.0	RT	9.4

4 Results

4.1 Analysis of the GIXD Measurements

4.1.1 Results for 13.2nm Samples

The thinnest sample films with a sufficient diffraction signal to index them are those with a frequency shift of 400Hz of the quartz microbalance. This corresponds to a nominal thickness of 13.2nm or 4.3 monolayers, calculated with the conversion factor r in equation 4.3. Here the results of three different series with this film thickness are demonstrated. For measuring condition see chapter 2.5 Grazing Incident Diffraction. Every picture had a measuring time of 3600 seconds. Figure 4.1 shows the measured and indexed reciprocal space map of the sample with low deposition rate, see table 3.1. The unit cell obtained by indexation in comparison to the surface induced phase of the spin coated films (which was used as a starting point) is given in table 4.1. A slight adjusting of the unit cell parameters was required with the result of a monoclinic unit cell.
The volume V = 1.43nm^3 was calculated by equation 1.2 leading to the electron density of 375nm^{-3} since there are two molecules in one unit cell with 536 electrons in total. Except the β value all parameters are very similar, pointing out the presence of a surface induced phase. This unit cell also features a monolayer height of

$$d_{ML} = c \cdot \sin(\beta) = 3.08nm \tag{4.1}$$

Again, in comparison a stretched out molecule has a length of 3.388nm [14]. The GIXD measurement of the heated substrate sample and those with a high deposition rate are plotted in figure 4.2 and 4.3. Both show the same spots as in figure 4.1, so the same unit cell is present. That implies the

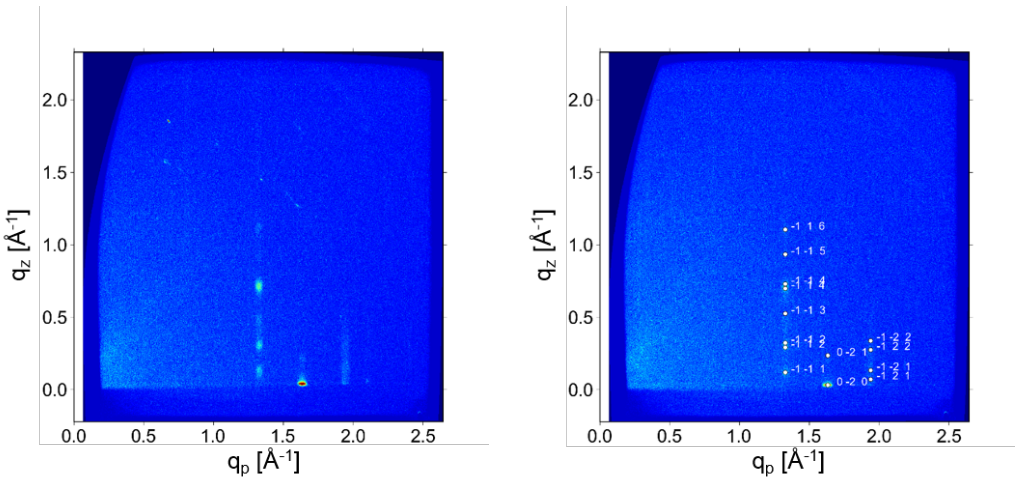

(a) (b)

Figure 4.1: (a) Experimental grazing incident diffraction patterns of the low deposition rate sample with a nominal thickness of 13.2nm measured at an incident angle of 0.135° and (b) with indexation of the Bragg peaks

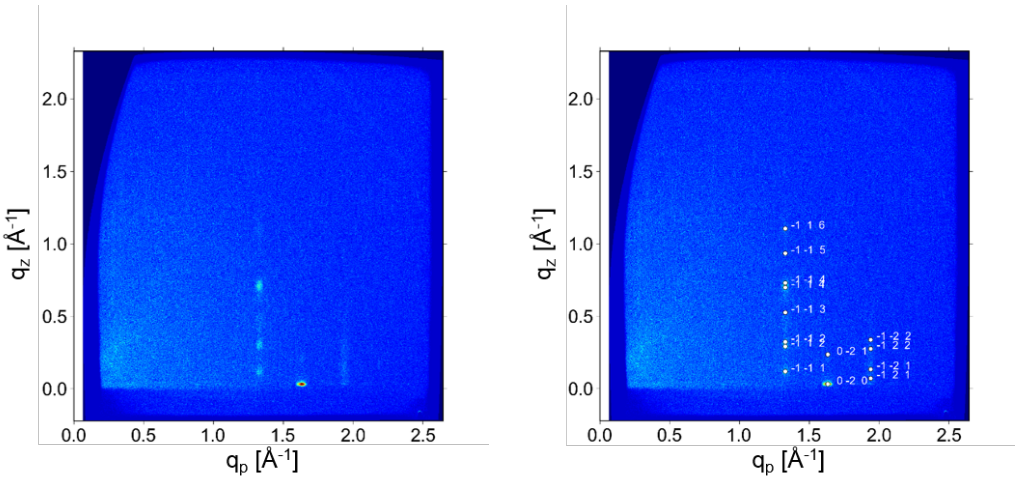

(a) (b)

Figure 4.2: (a) Experimental grazing incident diffraction patterns of the sample with heated substrate and a nominal thickness of 13.2nm measured at an incident angle of 0.130° and (b) with indexation of the Bragg peaks

molding of a surface induced phase up to a nominal thickness of 13.2nm by physical vapor deposition, independent of the deposition conditions.

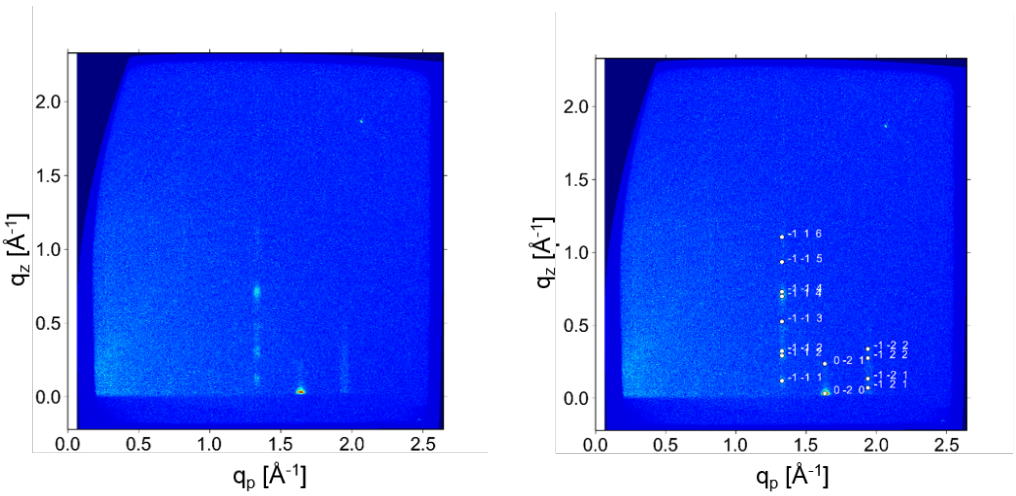

(a) (b)

Figure 4.3: (a) Experimental grazing incident diffraction patterns of the sample with high deposition rate and a nominal thickness of 13.2nm measured at an incident angle of 0.132° and (b) with indexation of the Bragg peaks

Table 4.1: Resulting unit-cell parameters by indexing with the program PyGid in comparison to the surface induced phase known from spin coating. One unit cell contains two molecules
V [nm^3] ... volume of the unit-cell calculated by equation 1.2
ρ_e [nm^{-3}] ... electron density

	a [Å]	b [Å]	c [Å]	α[°]	β[°]	γ[°]	V [nm^3]	ρ_e [nm^{-3}]
By indexing	6.0	7.7	31.0	90.0	95.5	90.0	1.43	375
Spin coated	6.02	7.75	31.08	90.0	97.0	90.0	1.44	373

4.1.2 Results for 99nm Samples

In the next step it was interesting to see whether a bulk phase would appear at thicker films of a frequency shift of 3000Hz meaning a nominal thickness of 99.0nm, or 32 monolayers. The three samples had the same deposition conditions as before and the same measuring conditions were used with a measuring time of 900 seconds per sample. The results are shown in figure

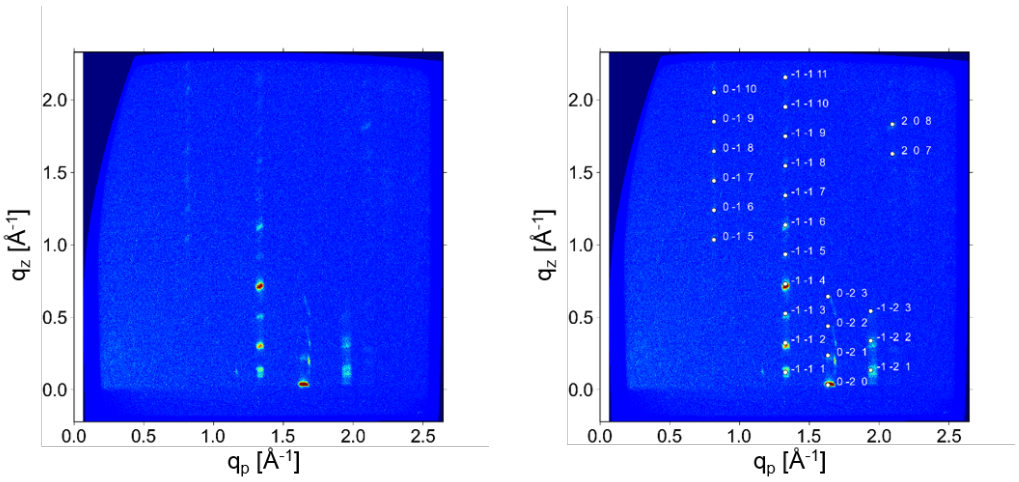

(a) (b)

Figure 4.4: (a) Experimental grazing incident diffraction patterns of the sample with low deposition rate and a nominal thickness of 99.0nm measured at an incident angle of 0.135° and (b) with indexation of the Bragg peaks

4.4, 4.5 and 4.6. Since there are more layers deposited the diffraction signal has a much higher intensity so clearly more spots are visible. Again, all three samples form the same unit cell and indexing leads to the parameters in table 4.1 equal to those of the 13.2nm specimen, meaning a surface induced phase occurs for films up to a film thickness of about 100nm, prepared by physical vapor deposition.

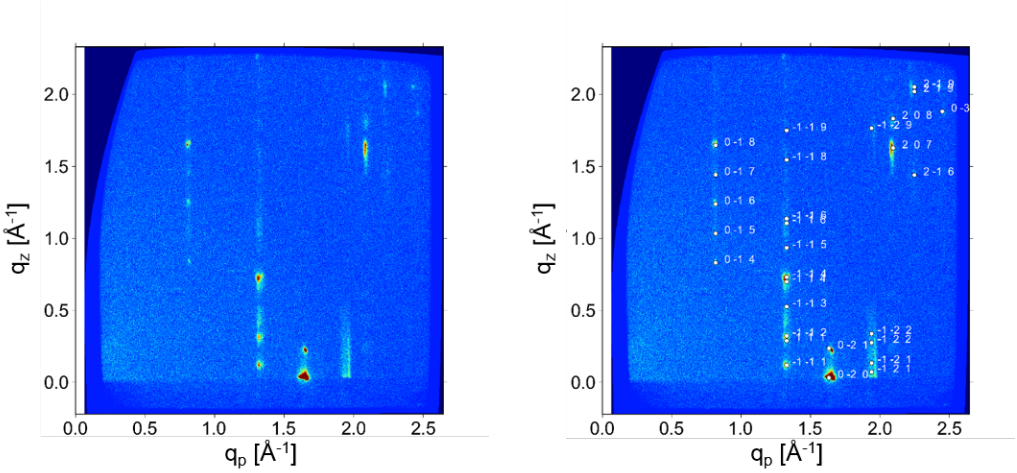

(a) (b)

Figure 4.5: (a) Experimental grazing incident diffraction patterns of the sample with heated substrate and a nominal thickness of 99.0nm measured at an incident angle of 0.135° and (b) with indexation of the Bragg peaks

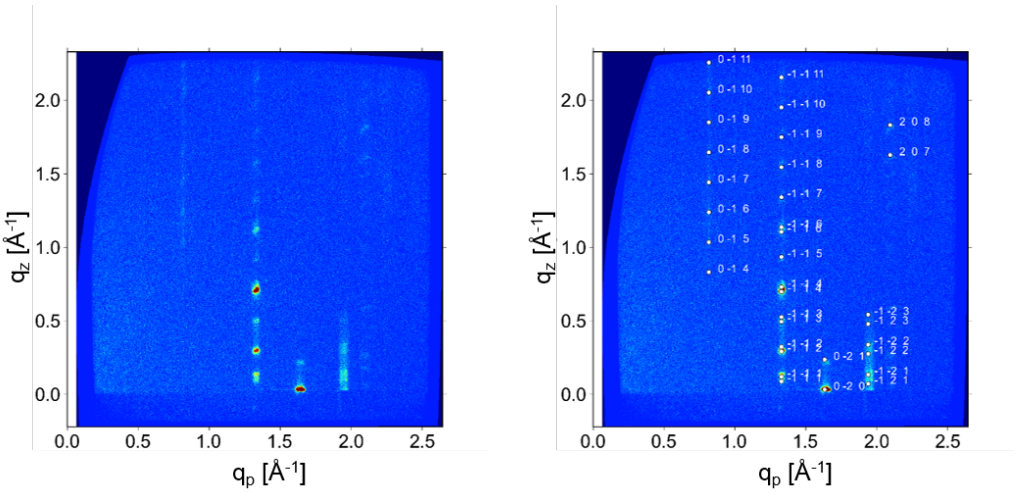

(a) (b)

Figure 4.6: (a) Experimental grazing incident diffraction patterns of the sample with high deposition rate and a nominal thickness of 99.0nm measured at an incident angle of 0.130° and (b) with indexation of the Bragg peaks

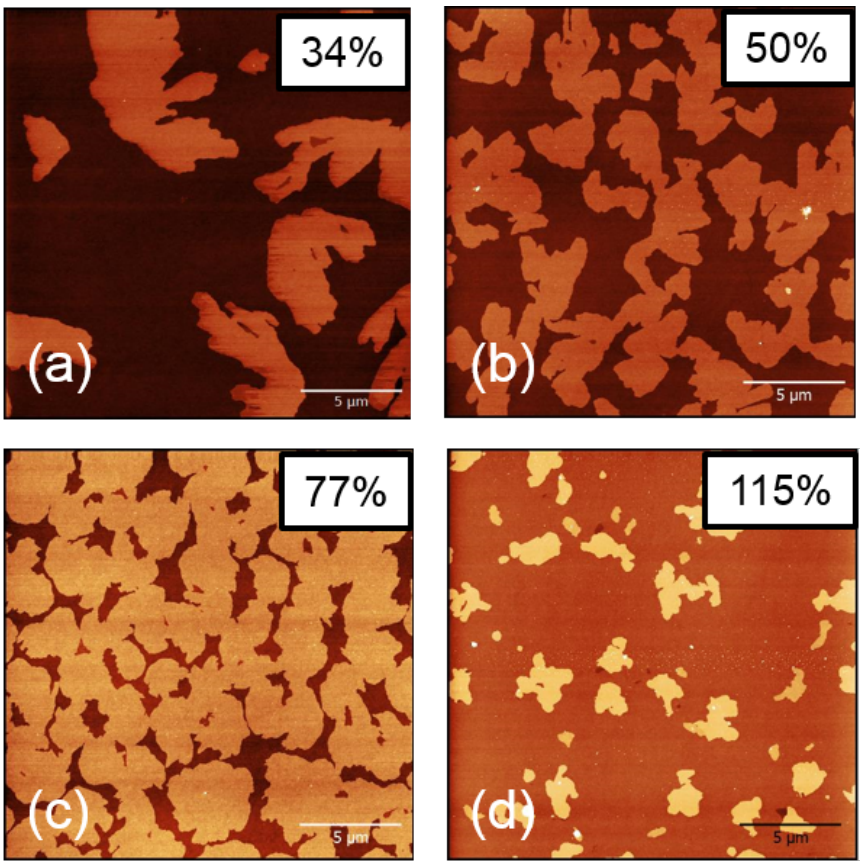

Figure 4.7: Atomic force microscopy measurements of the low deposition rate series sub-monolayers. The percentage of the coverage is determined by AFM

4.2 Morphology of Sub-Monolayers

The analysis of C_8O-BTBT-OC_8 sub-monolayers is especially interesting, since they couldn't be successfully prepared so far with spin coating. AFM measurements were taken to determine the morphology of films made with different deposition conditions. These measurements were then compared with XRR-fits.

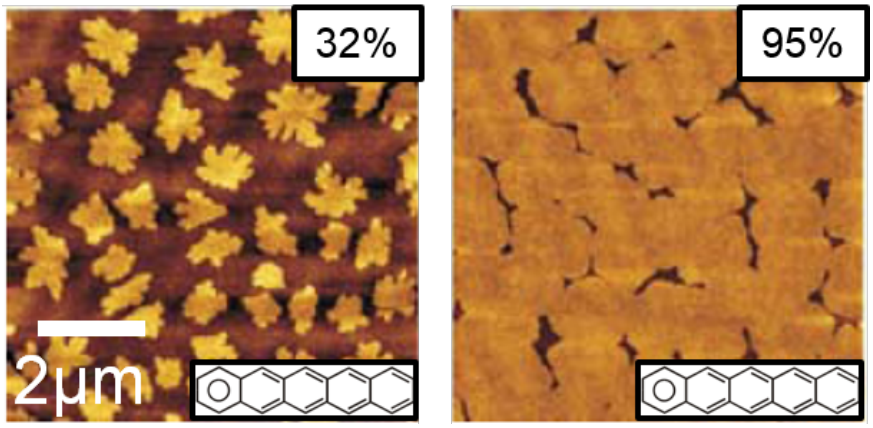

Figure 4.8: Atomic force microscopy measurements of pentacene prepared by physical vapor deposition and the chemical structure of a pentacene molecule. The percentage of the coverage is determined by AFM [32]

4.2.1 AFM Analysis

The island growth of the first sample series is illustrated by the topographic AFM images in figure 4.7. The islands have a quite fractal shape and start to interconnect with each other at a rather low coverage in the range of 50%. For comparison, figure 4.8 shows AFM measurements of pentacene ($C_{22}H_{14}$). This planar molecule composed of five linked benzene rings (also shown in figure 4.8) is a model system for studies of organic semiconductor film growth. The processes involved in pentacene film formations are discussed and recent experimental and numerical growth studies are reviewed [33]. The pentacene sub-monolayers are also produced by physical vapor deposition at similar conditions on 200nm thermally grown SiO_x. C_8O-BTBT-OC_8 in comparison has a much bigger domain size and the pentacene islands have a more fractal shape.

The four different sample series are compared in figure 4.9 to demonstrate the influence of the deposition condition on the island growth. All samples have a coverage of approximately 50%. Heating the substrate increases the domain size. Also sputtering has an effect on the diffusion process since the unsputtered sample has clearly smaller islands than the sputtered one, even though it has the same deposition conditions. The sample of the fourth se-

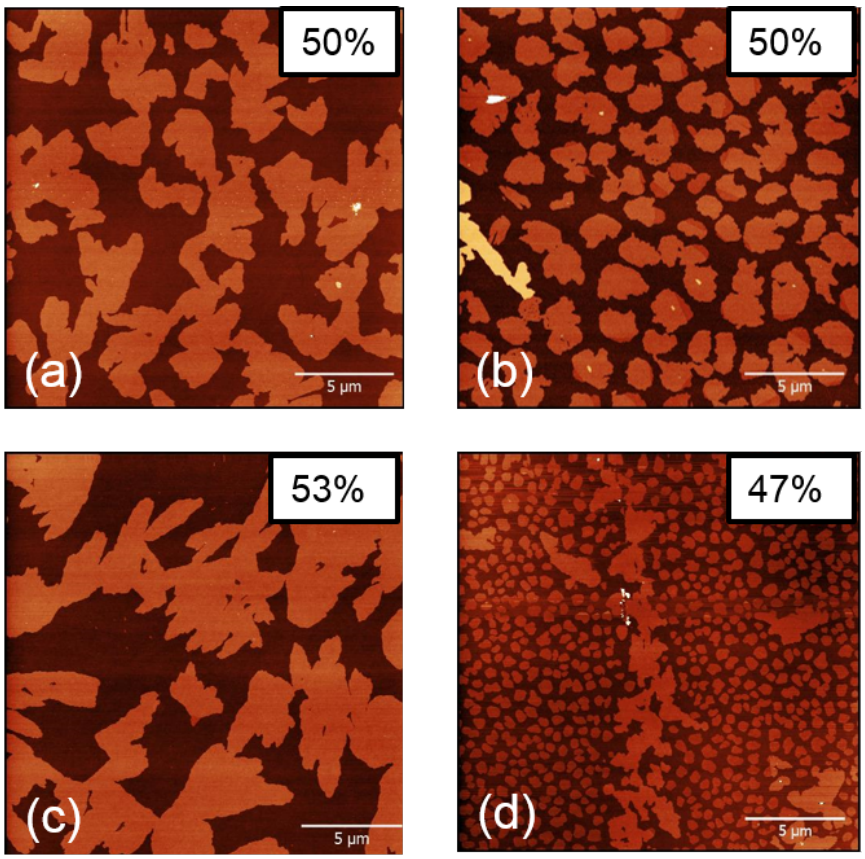

Figure 4.9: Atomic force microscopy measurements of all series of sub-monolayer samples of approximately equal coverage. For the deposition conditions see table 3.1. (a) is the sample of the low deposition rate series (b) of the unsputtered series, (c) shows the measurement of a heated substrate series and the fourth sample (d) is the one of the high deposition rate series

ries shows, increasing the deposition rate drastically lowers the domain size.

Since the GIXD measurements features a unit cell with an island height of d_{ML}=30.8Å, the coverage of the AFM delivers a nominal thickness

$$d_n = Cov_{AFM} \cdot d_{ML}. \tag{4.2}$$

The average calculated by the sum of all nominal thicknesses d_k of the sub-monolayers in table 4.2 divided by the corresponding frequency shift of

Table 4.2: Frequency shift of the quartz microbalance (QMB), measured coverage Cov_{AFM} and calculated nominal thickness d_n by equation 4.2 of the sub-monolayer samples of the first series and of the heated second series. The nominal thickness calculated by the conversion factor and the frequency shift deliver an estimated value $d = Hz \cdot r$

Series	QMB shift [Hz]	Cov_{AFM}	d_n [nm]	Hz · r [nm]
low deposition rate	35	34	1.12	1.2
	50	50	1.60	1.7
	75	77	2.40	2.5
	100	115	3.54	3.3
heated substrate	25	29	0.90	0.8
	50	53	1.62	1.7
	75	93	2.85	2.5
	100	109	3.34	3.3

the quartz microbalance Hz_k lead to a conversion factor

$$r = \sum_{k=1}^{N} \frac{d_k}{Hz_k \cdot N} = 0.33 \frac{\text{Å}}{Hz}, \tag{4.3}$$

so a complete monolayer (d_n=3.08nm) is achieved by a frequency shift of 93Hz. The samples are labeled by the nominal thickness calculated by this conversion factor (see table 3.1).

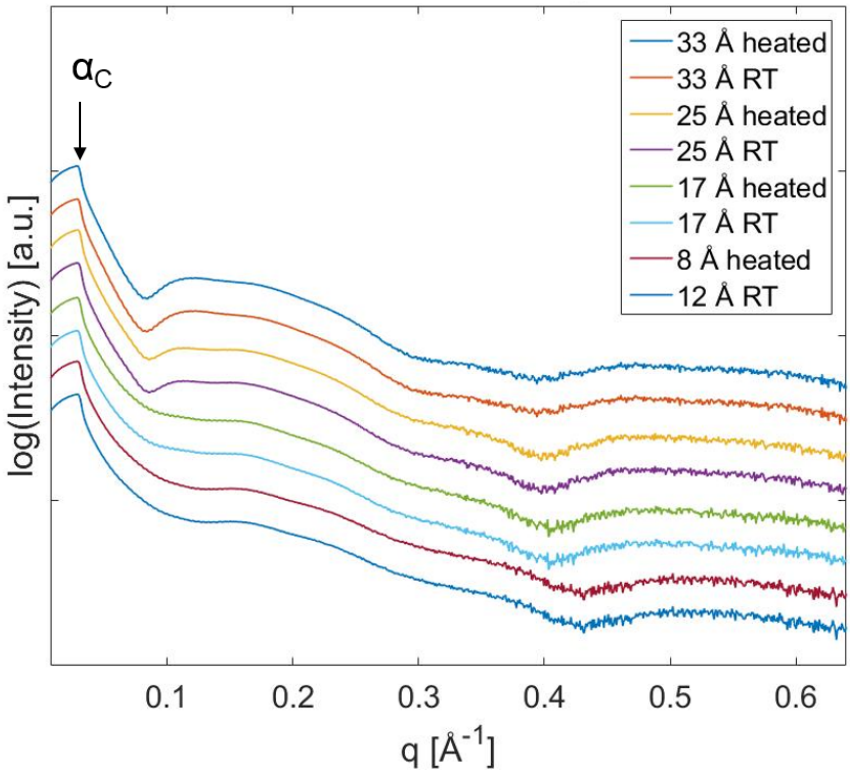

Figure 4.10: Waterfall-plot of all samples of the first series with low deposition rate and the second series with heated substrates shown in table 4.2

4.2.2 XRR Results

The fit of the XRR measurements were done only with the software *Stochfit*, since *X'Pert Reflectivity* showed no unique results for sub-monolayers. The molecule is divided into three parts, the two alkyl-sidechains and the BTBT core. The results of the GIXD measurements for a whole monolayer and the given values of the core [34] deliver density and height of the sidechains shown in table 4.3. These parameters make the AFM measurements via the coverage comparable to the fit results and provide a good start for the X'Pert Reflectivity program later on.

Figure 4.10 is a waterfall plot of all reflectivity curves of the low deposition rate and the heated substrate series. The critical angle α_C=0.218°obtained by the XRR measurements leads to an electron density calculated by equa-

Table 4.3: Thickness and density of the different molecule parts
ρ [g/cm^3] ... mass density
ρ_e [nm^{-3}] ... electron density
d[nm] ... layer thickness

	ρ[g/cm^3]	ρ_e [nm^{-3}]	d [nm]
Whole layer	1.15	375	3.08
Core [34]	1.60	520	1.17
Alkylchain	0.87	282	0.95

tion 2.4 and 2.6

$$\rho_e = \frac{\alpha^2 \pi}{\lambda^2 r_e} = 677 nm^{-3}, \tag{4.4}$$

which is very similar to the literature value of SiO_x, $\rho_e = 670\text{nm}^{-3}$ [35]. The curves of the heated sample and those at room temperature have a similar appearance. The higher the coverage, the clearer the minimum at q=0.1Å shows up.

Figure 4.11 illustrates the sub-monolayer regime showing the comparison of the AFM results and those of *Stochfit* XRR fits for the first sample series with low deposition rate and the heated substrate sample series. The coverage of the XRR fits were calculated by integrating the electron density profile and dividing it with the density of a monolayer (equation 4.5) For samples with low coverage, both results are quite similar, whereas well covered samples show different result for both methods.

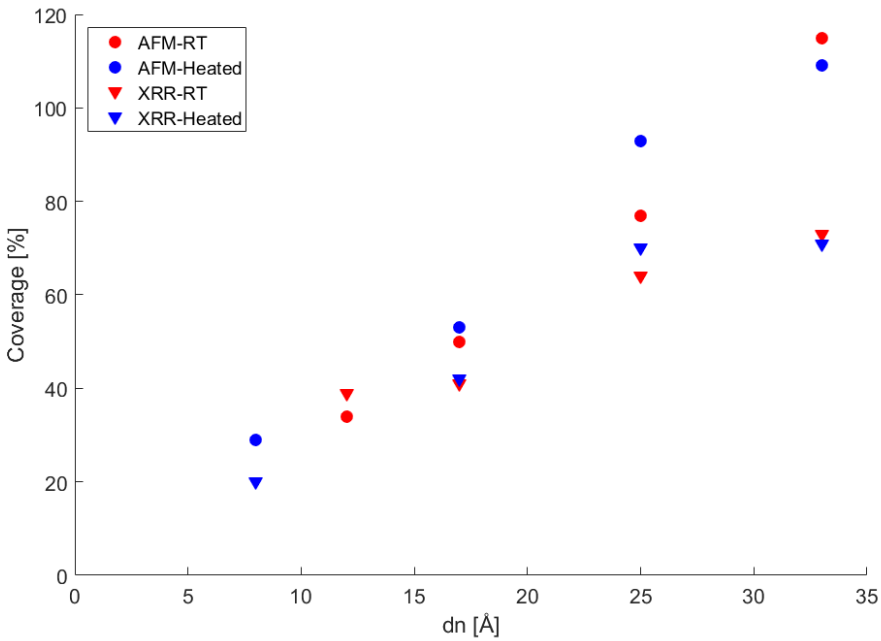

Figure 4.11: Comparison of atomic force microscopy and X-ray reflectivity fit results for the coverage depending on the nominal thickness d_n (see table 4.2)

4.2.3 Examples

Sample with 1.7nm and low deposition rate

Figure 4.12 shows the fit of the *Stochfit* program of the first series sample with a nominal thickness of d_n=1.7nm (AFM micrograph imaged in figure 4.7b), with the resulting electron density profile plotted in figure 4.13. The dashed lines are the expected values calculated with the coverage of the AFM measurement (50%) and the data of table 4.3 for the different parts of the molecule. According to that the core has an electron density $\rho_e = 260\text{nm}^{-3}$ and the alkyl sidechains $\rho_e = 141\text{nm}^{-3}$, so all together the layer has a density of $\rho_e = 188\text{nm}^{-3}$. Since *Stochfit* only calculates normalized electron densities, the known value of the SiO_xsubstrate $\rho_e = 670\text{nm}^{-3}$ was taken as a reference to calculate the absolute densities. For the fit an input of 3nm for the layer thickness was used divided into 60 boxes. The result for the electron density of the sub-monolayer is $\rho_{e,Fit} = 153\text{nm}^{-3}$, so compared

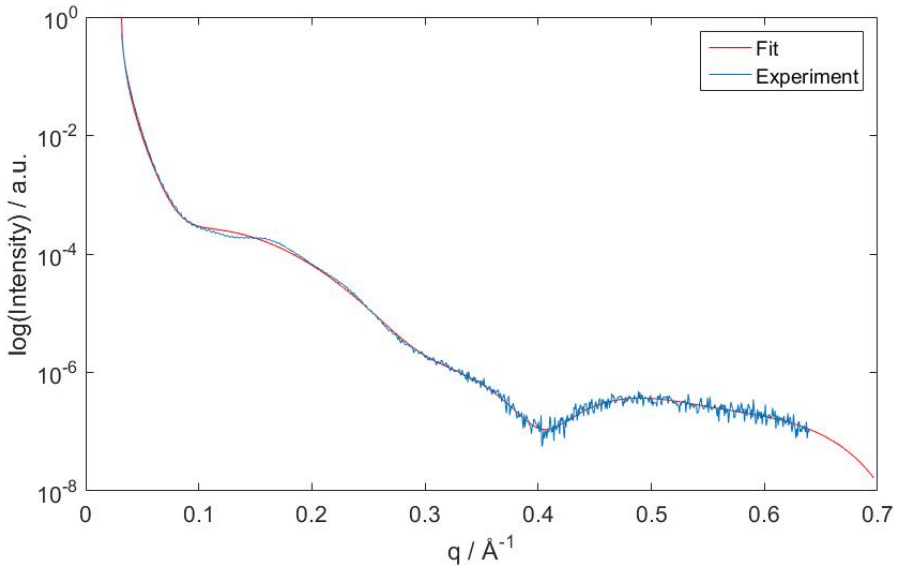

Figure 4.12: Fit of the measured X-ray reflectivity data with *Stochfit* for the sample with low deposition rate and a nominal thickness of 1.7nm

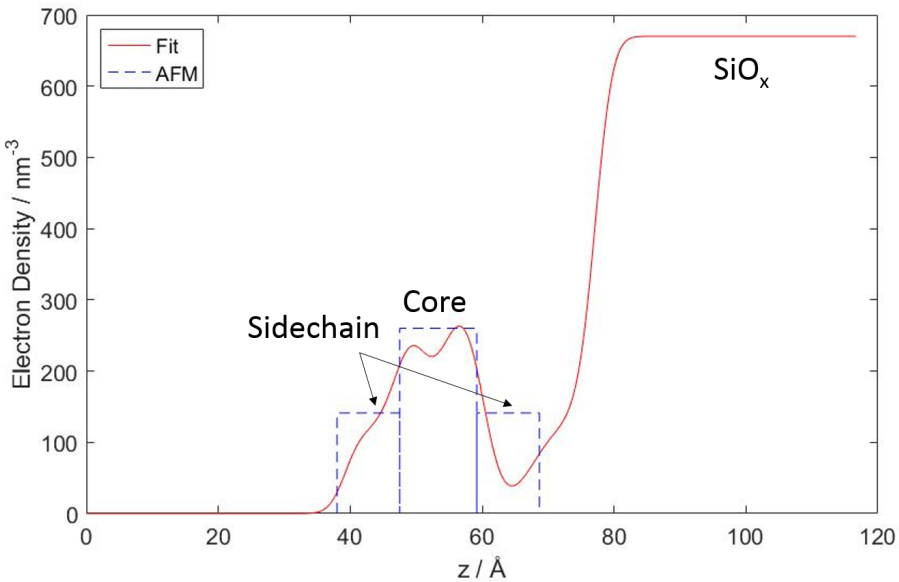

Figure 4.13: Electron density profile by *Stochfit* of the sample with low deposition rate and a nominal thickness of 1.7nm. The dashed lines are the expected values of the atomic force microscopy measurement for the core and the two alkyl sidechains. SiO_x is the substrate.

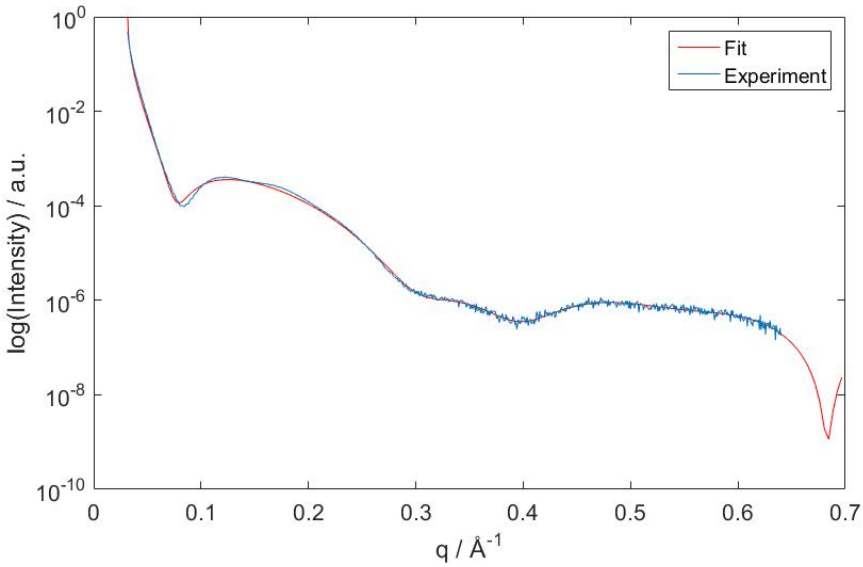

Figure 4.14: Fit of the measured X-ray reflectivity data with *Stochfit* for the sample with low deposition rate and a nominal thickness of 3.3nm

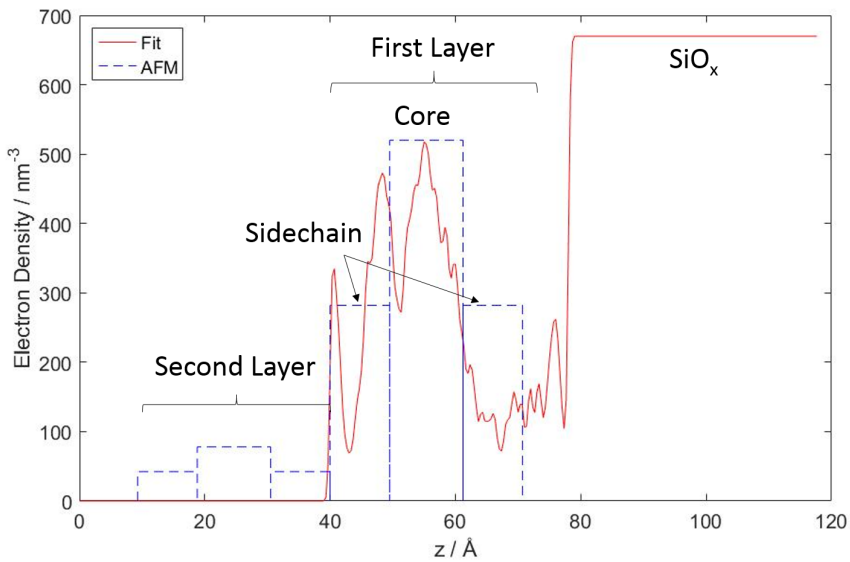

Figure 4.15: Electron density profile by *Stochfit* of the sample with low deposition rate and a nominal thickness of 3.3nm. The dashed lines are the expected values of the atomic force microscopy measurement for the core and the two alkyl sidechains. SiO_x is the substrate.

to ρ_e of a filled monolayer of table 4.3 as a reference, that means a coverage

$$Cov = \frac{\rho_{e,Fit}}{\rho_{e,Ref}} = 41\% \tag{4.5}$$

which is in good agreement with the AFM measurement.

Sample with 3.3nm and low deposition rate

The next sample is 3.3nm thick, again from the low deposition rate series (figure 4.14 and 4.15). Here the AFM measurement, depicted in figure 4.7c, delivers a coverage of a filled first layer with an electron density according to table 4.1 of 375nm^{-3} and the appearance of a second layer with 15% leading to a density of 56nm^{-3}. These layers again can be divided into the core and the two attached sidechains calculated with the values of table 4.3. For the fit with *Stochfit* again an input of 3nm for the layer thickness and 60 boxes are used. In the result only the first layer shows up with an electron density of 272nm^{-3} and by equation 4.5 a coverage of 73%.

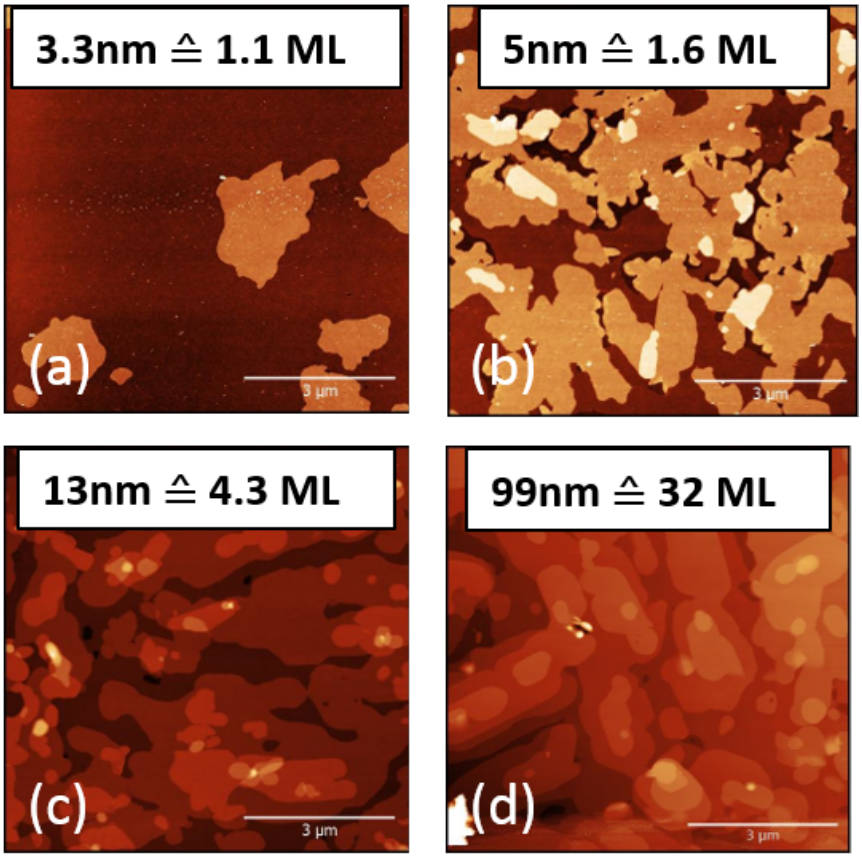

Figure 4.16: Atomic force microscopy measurements of the low deposition rate samples with 1.1 to 32 monolayers of deposited material. In (a) and (b) the roughness still increases with the deposition, whereas in (c) and (d) the roughness stays constant and only 3 to 4 partial layers can be distinguished.

4.3 Morphology of Multilayers

In the last part of this thesis we now take a look at the layer growth for thicker films up to 32 monolayers.

4.3.1 AFM Analysis

Again it is interesting to see the comparison of the AFM measurements between C_8O-BTBT-OC_8 and pentacene, so figure 4.16 shows the AFM micrographs for the samples of the low deposition rate series from 1.1 to 32 monolayers.

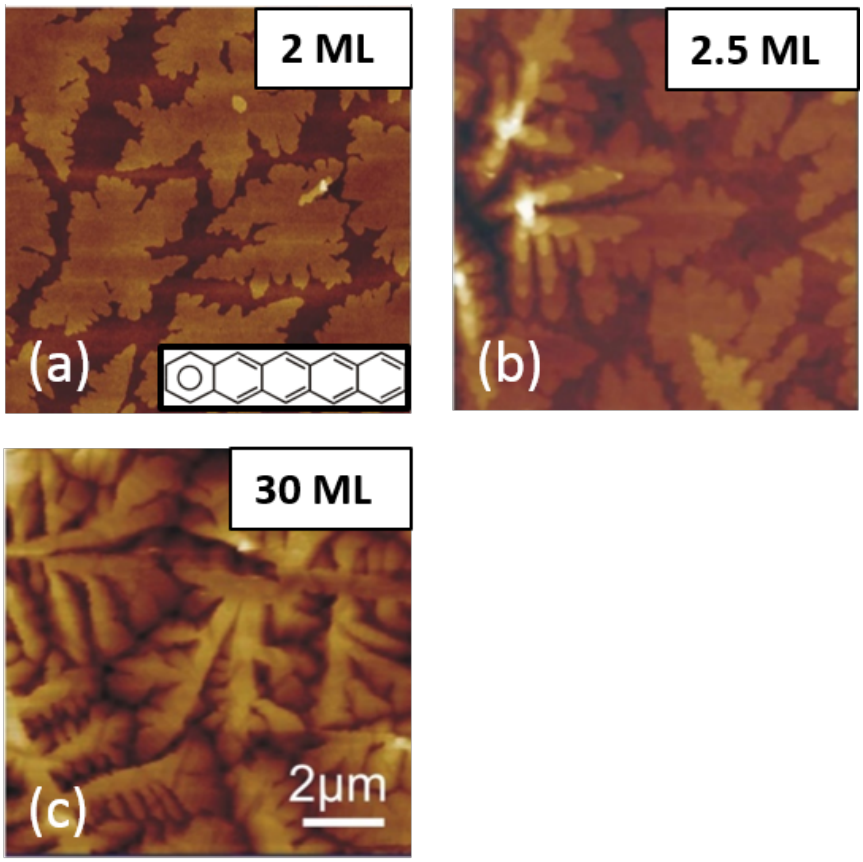

Figure 4.17: Atomic force microscopy measurements of the pentacene films by physical vapor deposition. [32]

It clearly exhibits a pronounced layer by layer growth and only the top 4 to 5 partial layers can be distinguished after enough material is deposited. This also has an effect on the roughness behavior.
In comparison to the pentacene films in figure 4.17 the roughness starts to increase constantly with the amount of deposited material, but in the case of C_8O-BTBT-OC_8 the roughening stops after a nominal layer thickness of 4 monolayers. However the roughness of the pentacene sample constantly increases and the islands have a more dendritic shape. In the latter case a very early bulk structure appears at a nominal thickness of about 50nm.

In figure 4.18 one sees the layer growth of the heated samples. The domain size of the partial layers is much bigger then for the samples kept at room

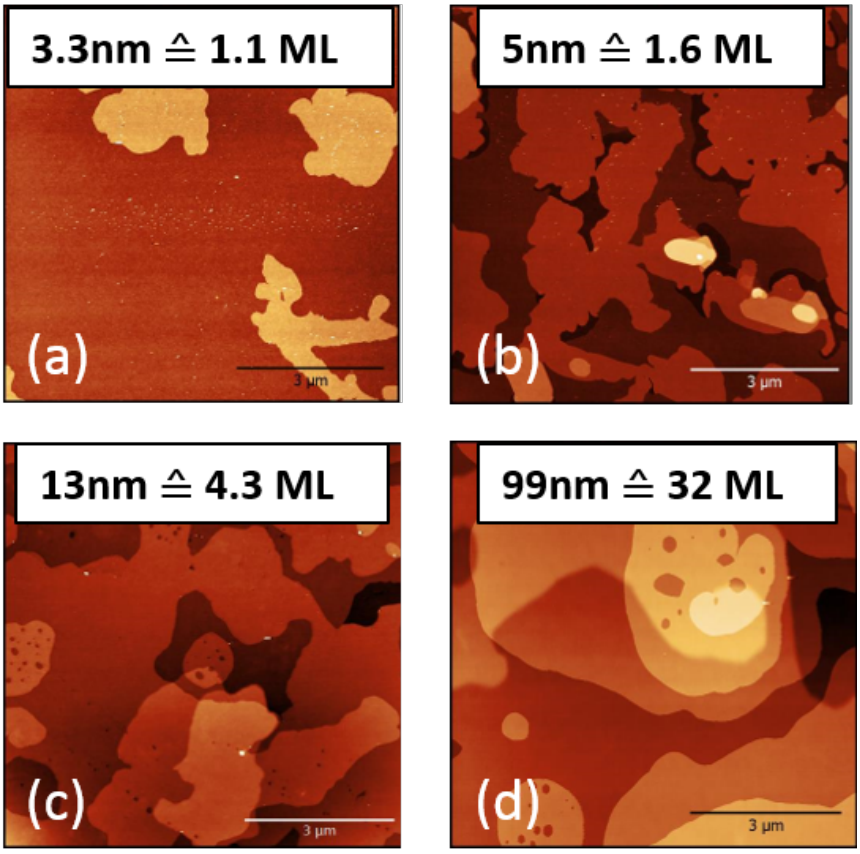

Figure 4.18: Atomic force microscopy measurements of samples prepared with heated substrates. The domain size of the islands is clearly bigger the for the unheated ones, like in figure 4.16

temperature in figure 4.16. Later the XRR measurements will show this also increases the roughness of those samples.

4.3.2 XRR Results

Figure 4.19 shows the XRR measurements of the low deposition rate series with a nominal thickness of 3.3 up to 99nm. Due to the interference of Bragg peaks and Kissig fringes, the measured peaks are shifted towards the Bragg peaks. The latter ones are indicated in table 4.4 and feature a d-spacing of d_{001}=3.08nm, which agrees perfectly with the GIXD unit cell in the 001 orientation (equation 4.1).

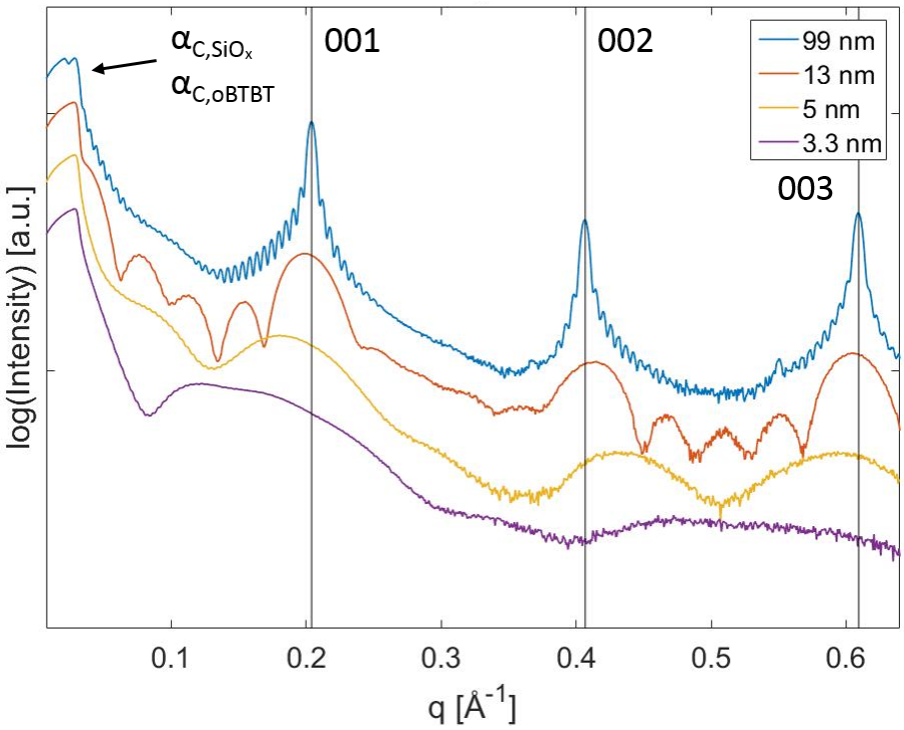

Figure 4.19: X-ray reflectivity measurements in a waterfall-plot of the low deposition rate series from a nominal thickness of 3.3nm up to 99nm. At the 99nm thick sample two critical angles appear, one concerning the SiOx material and the other one to the C_8O-BTBT-OC_8, since the amount of deposited material is enough for the appearance

Table 4.4: Measured Bragg peaks featuring a d-spacing of d_{001} = 3.08nm

Peak	q [Å^{-1}]
001	0.204
002	0.407
003	0.609

Also the critical angle of the C_8O-BTBT-OC_8 material appearing at the 99nm thick sample, $\alpha_{C,oBTBT}$=0.163°, leading to an electron density ρ_e=378nm^{-3} is very similar to the GIXD result. The second critical angle, again at α_{SiO_x}=0.163°, meaning an electron density of ρ_e=677nm^{-3} is a good result comparing to the literature value of ρ_e=670nm^{-3}.

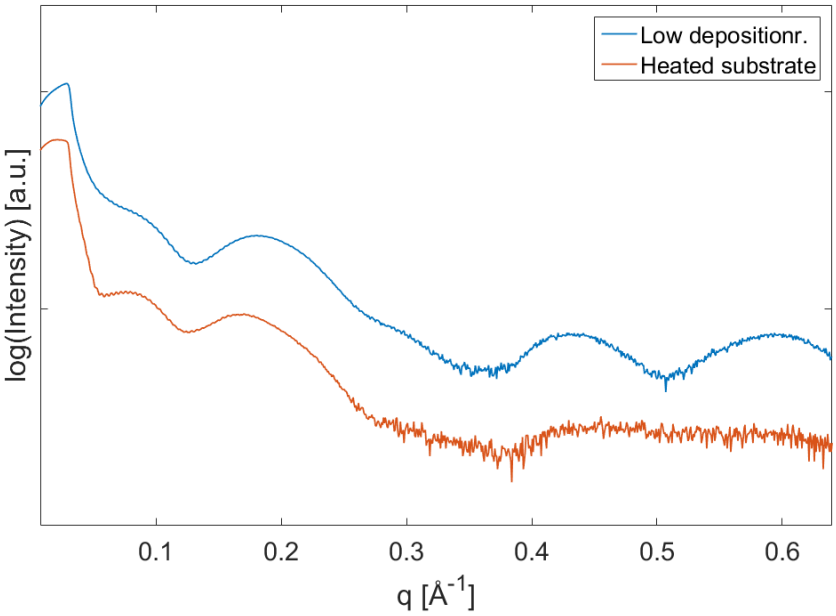

Figure 4.20: X-ray reflectivity measurements in a waterfall-plot of samples prepared with low deposition rate and heated substrate, both with a nominal thickness $d_n = 5.0$nm.

4.3.3 Examples

Sample with 5.0nm and heated substrate

Figure 4.20 shows a comparison of the measured XRR curves for the sample of the low deposition rate series and the heated substrate series, both with a nominal thickness of 5nm. The results for the latter sample will be explained below.

The measured AFM plot in figure 4.21 shows the appearance of basically three partial layers, and layer A, the substrate. These layers have a coverage of $Cov_B = 94\%$, $Cov_C = 63\%$ and $Cov_D = 6\%$. Layer E and F can be neglected. With these values and the layer height d_{ML} of the GIXD measurements in equation 4.1, the nominal thickness

$$d_{n,AFM} = \sum_{n}^{N} Cov_n \cdot d_{ML} = 5.02nm \tag{4.6}$$

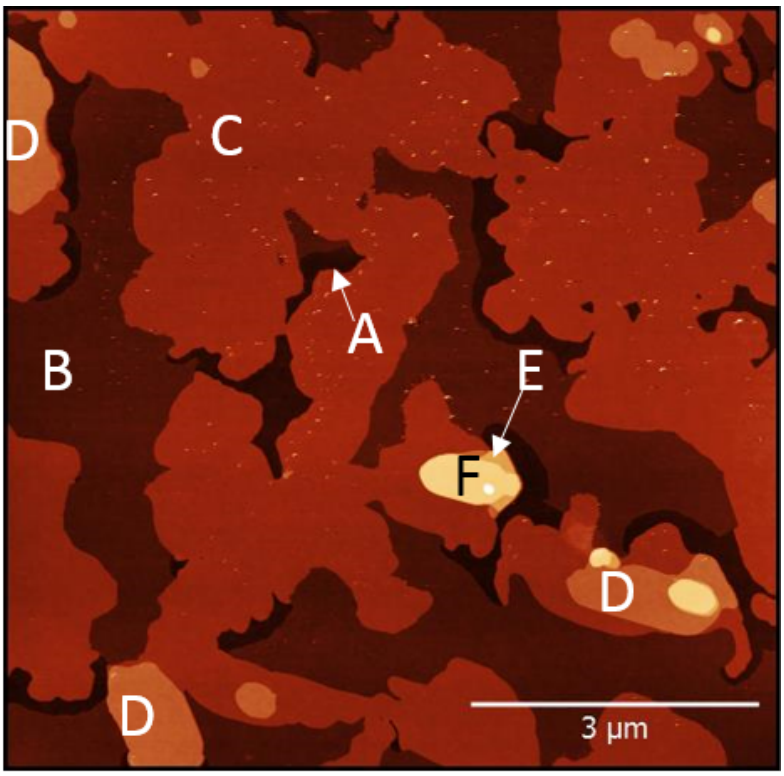

Figure 4.21: The atomic force microscopy micrograph of the 5nm sample of the heated series shows the appearance of basically 4 layers. Layer A is the substrate.

follows. This is in very good agreement with the estimated value d_n = 4.95nm calculated with the conversion factor r of equation 4.3 and the frequency shift of the quartz microbalance.

The resulting electron density profile by *Stochfit* is depicted in figure 4.22 and 4.23. The best fit results were achieved with the input thickness of 6nm divided into 120 boxes. In the fit only the first two layers show up. Thus Layer B has an electron density of $\rho_e = 350\text{nm}_{-3}$ leading via the values in table 4.3 and equation 4.5 to a coverage of $\text{Cov}_{B,Fit} = 94\%$, which exactly the same result as the AFM measurement. According to the fit the electron density of Layer C is $\rho_e = 180\text{nm}_{-3}$, meaning a coverage of $\text{Cov}_{C,Fit} = 48\%$, which is in good agreement to the AFM result.

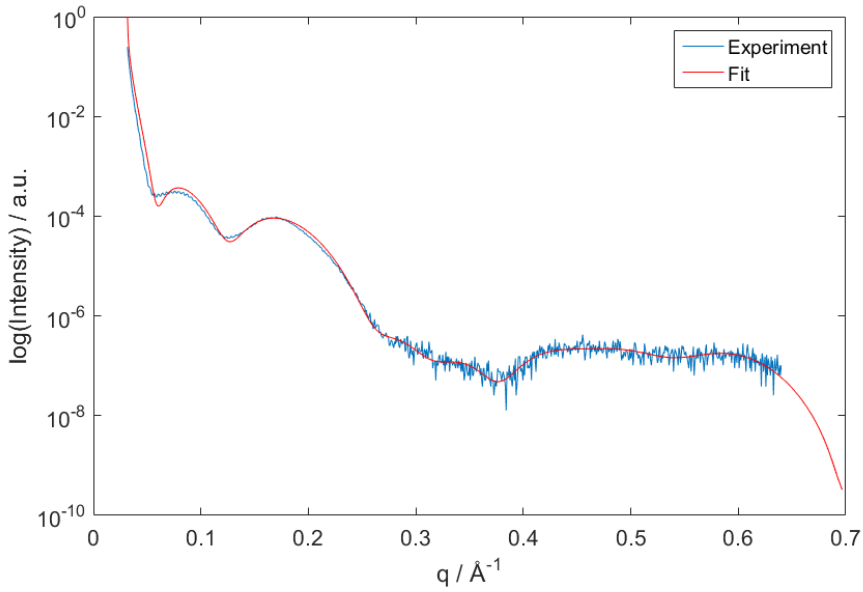

Figure 4.22: Fit of the measured X-ray reflectivity data with *Stochfit* of the sample with heated substrate and a nominal thickness of 5.0nm

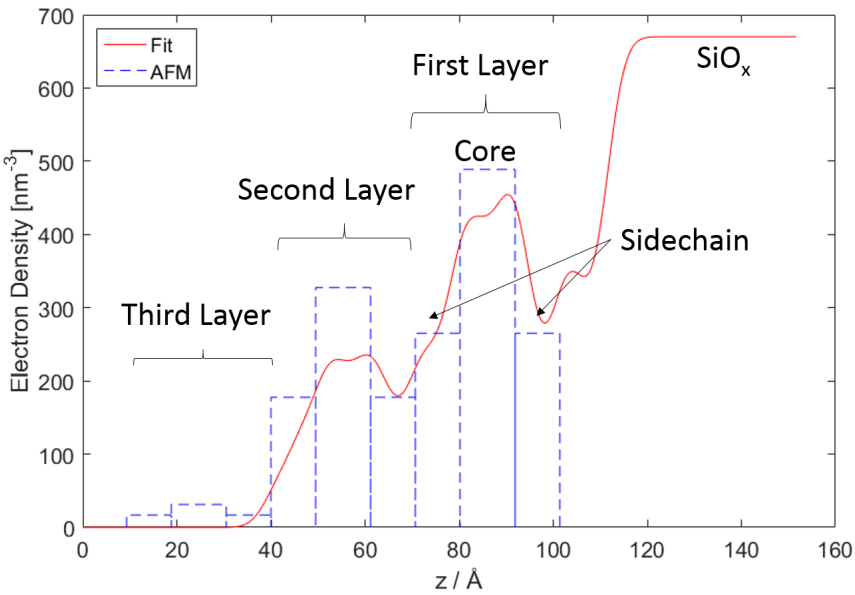

Figure 4.23: Electron density profile resulting of the fit with *Stochfit* of the sample with heated substrate and a nominal thickness of 5.0nm. The dashed lines are the expected values of the atomic force microscopy measurement for the core and the two alkyl sidechains. SiO_x is the substrate.

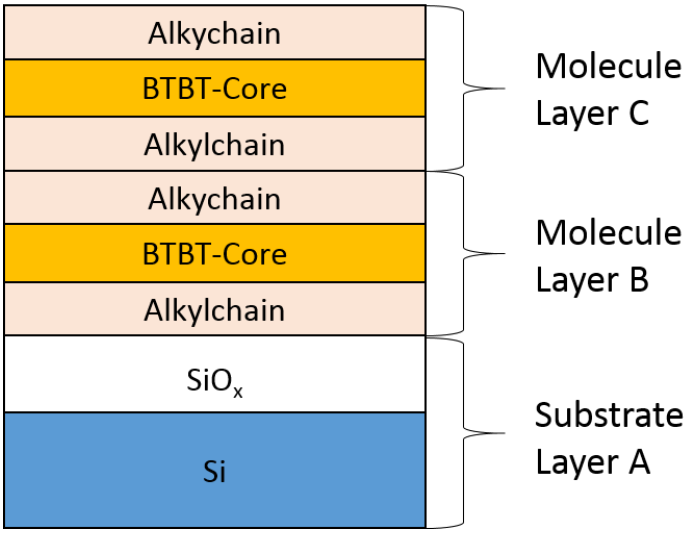

Figure 4.24: Schematic layer model for the *X'Pert reflectivity* fit

In figure 4.24 the fit model for the *X'Pert Reflectivity* program is schematically pictured. The two simulated layers are divided in its three parts. The AFM values were taken for the start. The fit is plotted in figure 4.25 including the illustration of the results in form of an electron density profile. The resulting values are also shown in table 4.5. This leads to a coverage of the second layer C $\mathrm{Cov}_C = 66\%$, almost the same as the AFM is showing and the first layer B $\mathrm{Cov}_B = 82\%$ is also in good agreement. The nominal thickness can be calculated with the coverage and the fitted thicknesses

$$d_{n,XR} = \sum_{n}^{N} Cov_n \cdot d_n = 4.26nm \tag{4.7}$$

It is quite similar to the estimated value 4.95nm.

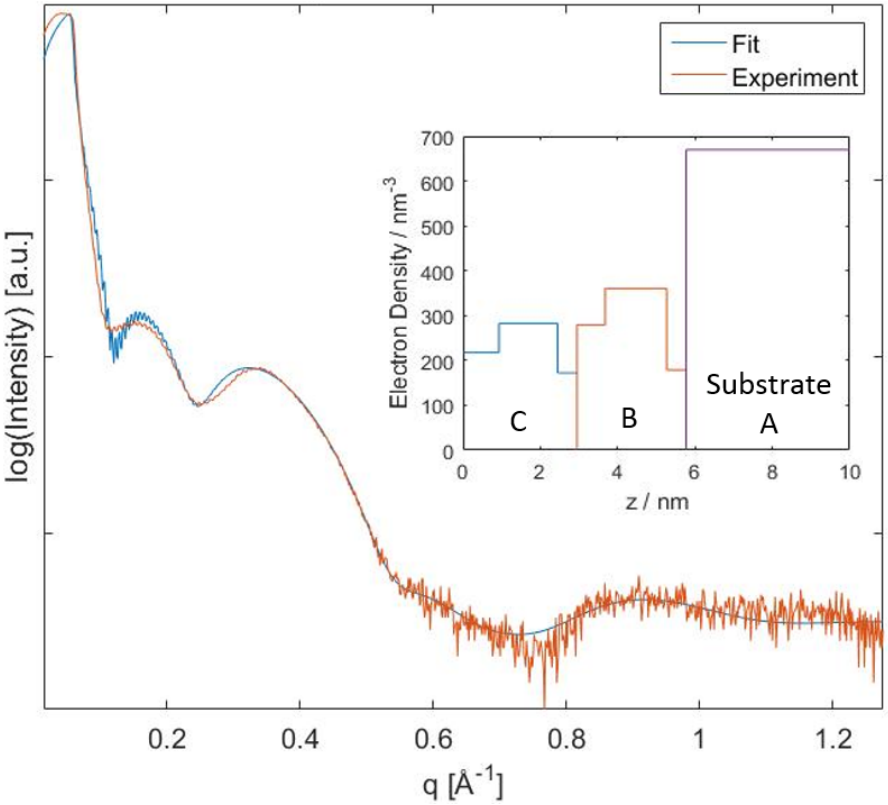

Figure 4.25: *X'Pert Reflectivity* fit of the X-ray reflectivity measurements and the resulting electron density profile of the sample with heated substrate and a nominal thickness of 5.0nm

Table 4.5: Result of the *X'Pert Reflectivity* fit. The letter in brackets is the belonging layer
ρ_e [nm^{-3}] ... electron density
d [nm] ... thickness

Layer	ρ_e [nm^{-3}]	d [nm]	Roughness [nm]
Alkylch. (C)	218	0.93	0.60
BTBT (C)	283	1.52	0.01
Alkylch. (C)	172	0.5	0.53
Alkylch. (B)	280	0.73	0.69
BTBT (B)	361	1.59	0.34
Alkylch. (B)	179	0.5	0.65
SiO_x (A)	618	180	1.65

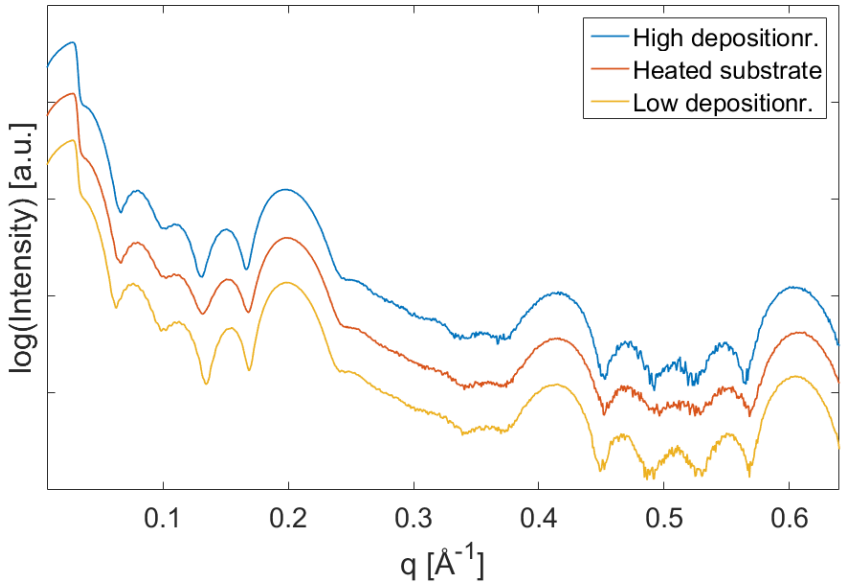

Figure 4.26: X-ray reflectivity measurements in a waterfall-plot of all three series with a nominal thickness of 13.2nm

Sample with 13.2nm and low deposition rate

Figure 4.26 is a waterfall plot of the XRR measurements of all series with a nominal thickness of 13.2nm. All measured graphs look very similar, with the Bragg peaks at the same positions. The Kiessig fringes of the heated sample are less pronounced than the others. This indicates a higher roughness for this sample. The 13.2nm sample with low deposition rate will be discussed below.

The cut through profile in figure 4.28 in position one of the AFM micrograph (figure 4.27) shows the appearance of only 3 partial layers. Since the complete bottom layer is also C_8O-BTBT-OC_8 this really means pronounced layer by layer growth, where the material tends to fill the layers rather then starting a new one.

At first the *Stochfit* results will be explained. The XRR fit with an input thickness of 15nm and 300 boxes is shown in figure 4.29. The corresponding electron density profil is plotted in figure 4.30. The dashed blue lines are

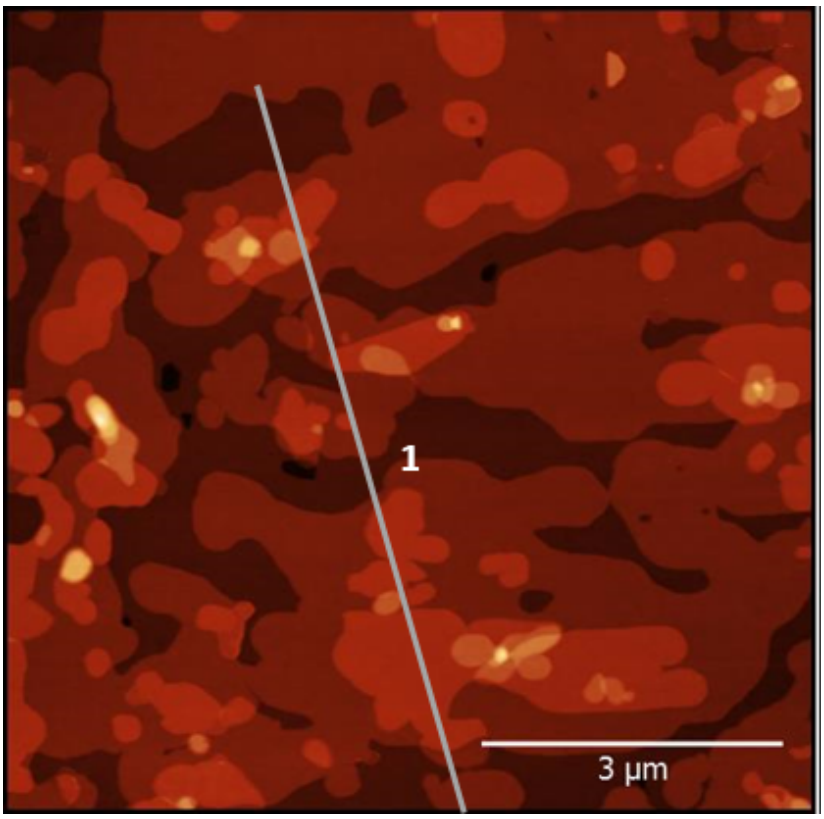

Figure 4.27: Atomic force microscopy micrograph of the low deposition rate sample with a nominal thickness of 13.2nm. The white line is the place of the cut through below

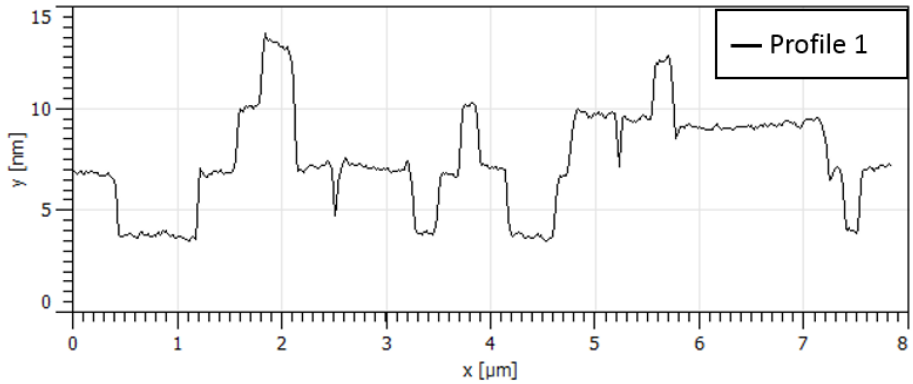

Figure 4.28: Height profile of the cut through the atomic force microscopy micrograph

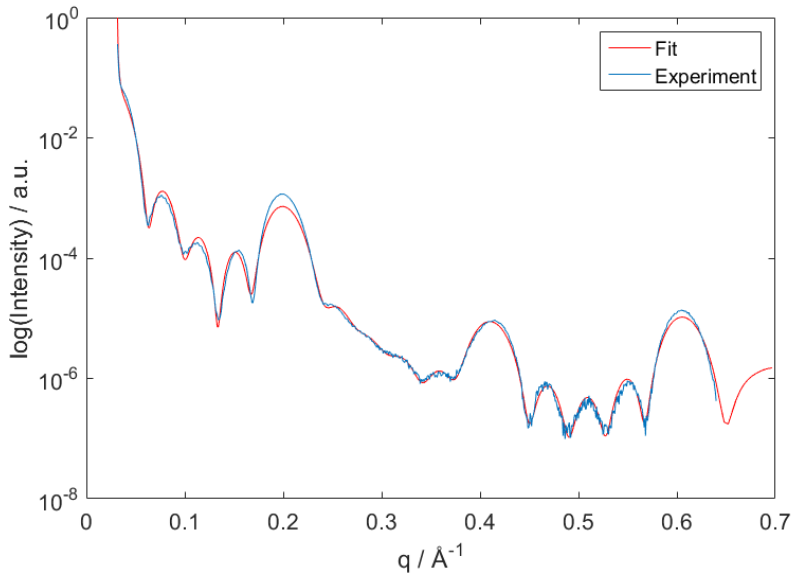

Figure 4.29: Fit of the measured X-ray reflectivity data by *Stochfit* for the sample with low deposition rate and a nominal thickness of 13.2nm

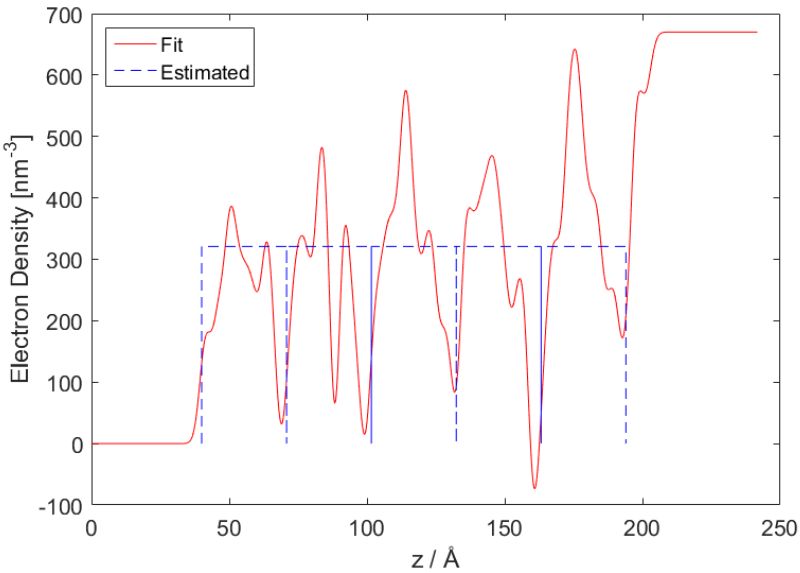

Figure 4.30: Electron density profile by *Stochfit* of the sample with low deposition rate and a nominal thickness of 13.2nm. The dashed lines are the estimated values calculated in equation 4.8. SiO_x is the substrate.

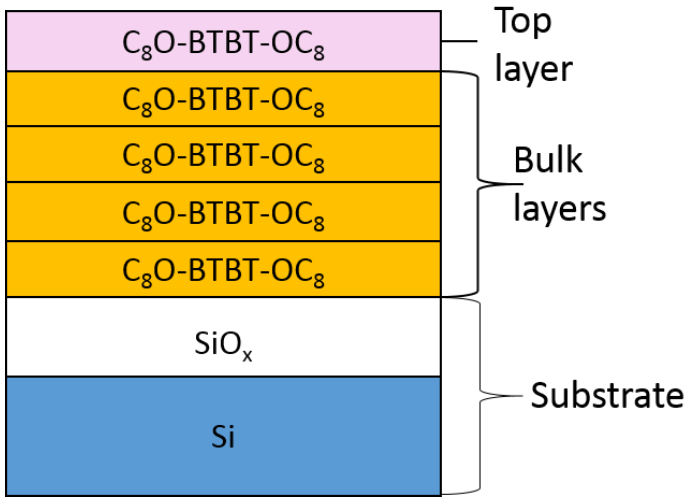

Figure 4.31: Schematic layer model for the *X'Pert reflectivity* fit

calculated by the nominal thickness of the quartz microbalance frequency shift d_n (see table 3.1), the absolute film thickness of 5 molecule layers d_{abs} with the height of one layer d_{ML} given by the GIXD measurement (equation 4.1) and the electron density for a filled monolayer ρ_e in table 4.1. So the estimated electron density equals

$$\rho_{est} = \rho_e \cdot \frac{d_n}{d_{abs}} = 321 nm^{-3} \tag{4.8}$$

with $d_{abs} = 5 \cdot d_{ML} = 15.4$nm. The density profile is split into two parts. The first four layers show the same behavior, so it was obvious to consider them being equal, that means taking the average of these layers. In the following these four layers are called bulk-layers. One bulk-layer now has an electron density of $\rho_e = 300\text{nm}^{-3}$, leading to an coverage of $\text{Cov}_{Bulk} = 80\%$. The left top layer has a clearly less density of only $\rho_e = 246\text{nm}^{-3}$ or a coverage of $\text{Cov}_{Top} = 66\%$. The measured thickness for all 5 layers is d_{fit} =3.06nm, which is very close to the GIXD result for d_{ML}(aforementioned). All together this leads to a nominal thickness of

$$d_{n,St} = \sum_n^N Cov_n \cdot d_n = 11.9nm \tag{4.9}$$

in good agreement to the expected value in table 3.1.

The fit-model for the *X'Pert Reflectivity* fit of the XRR data is depicted in figure 4.31. To keep the number of parameters low the property of one bulk-layer is copied 4 times. A separate top layer and the parameters for the substrate are also included in the fit. As start values, the *Stochfit* results are chosen. This lead to a fit shown in figure 4.32. Also the results in table 4.6 are plotted in the form of an electron density profile. The nominal thickness concerning the values in table 4.6 can now be calculated in the same way, with equation 4.9 leading to $\mathrm{d}_{n,XR} = 12.1\mathrm{nm}$.

Both fit softwares, *Stochfit* and *X'Pert Reflectivity* show almost the same results, so they are very accurate for this film thickness.

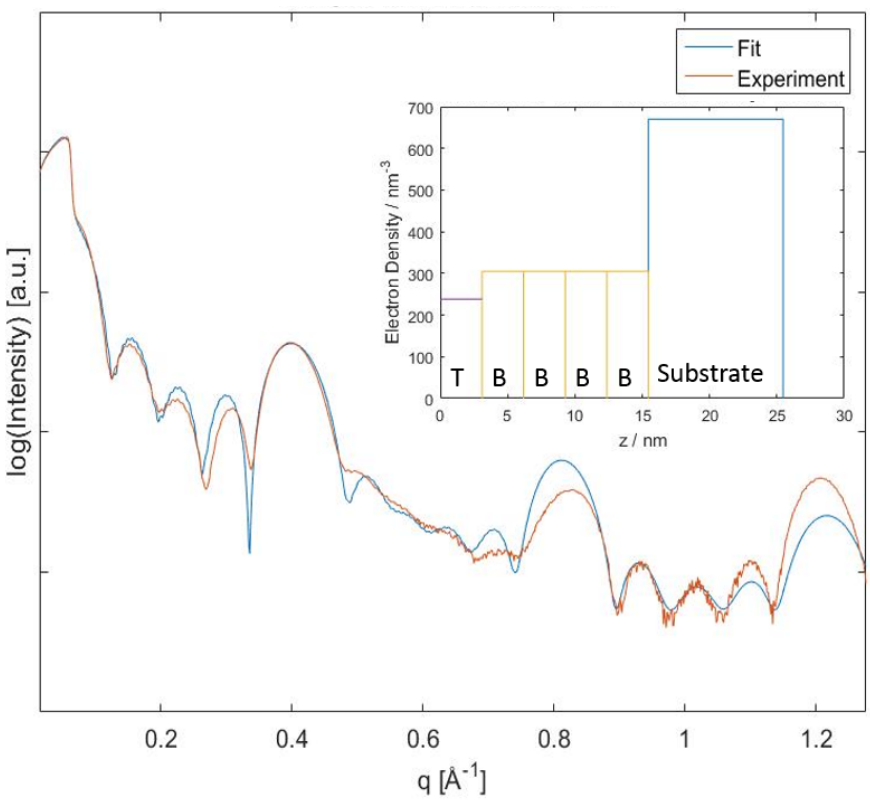

Figure 4.32: *X'Pert Reflectivity* fit of the X-ray reflectivity measurement and the resulting electron density profile of the sample with low deposition rate and a nominal thickness of 13.2nm

Table 4.6: Result of the *X'Pert Reflectivity* fit for the sample with low deposition rate and a nominal thickness of 13.2nm
ρ_e [nm^{-3}] ... electron density
d [nm] ... thickness
Cov [%] ... coverage (for the calculation see equation 4.5)

Layer	ρ_e [nm^{-3}]	d [nm]	Roughness [nm]	Cov [%]
Top	239	3.10	0.55	64
Bulk (4x)	305	3.09	0.20	82
SiO_2	731	136	0.21	-

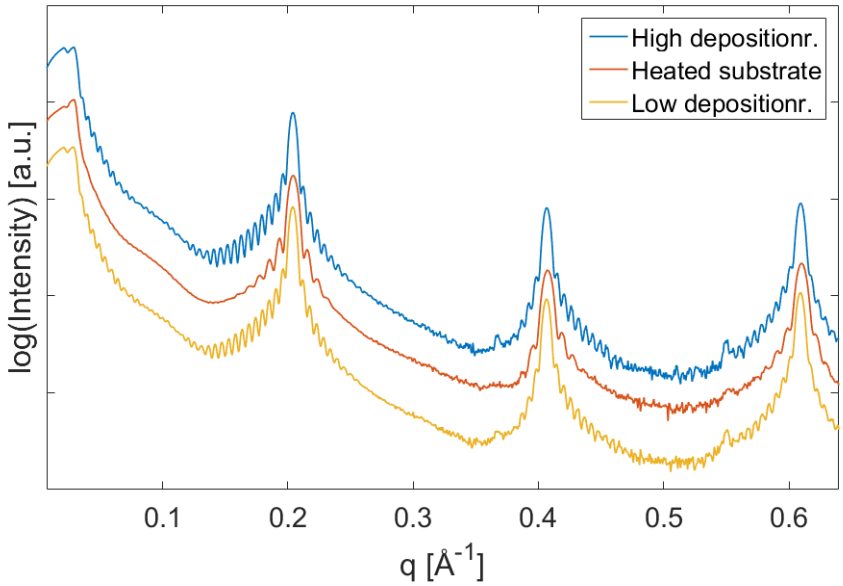

Figure 4.33: X-ray reflectivity measurements in a waterfall-plot of all three series with a nominal thickness of 99nm

Sample with 99nm and low deposition rate

In figure 4.33 a waterfall plot of the XRR measurements of all series with a nominal thickness of 99nm is shown. The curves look very similar, all with the same Bragg peaks. There are no visible Kiessig fringes for the heated sample, so like the 13.2nm example this series also shows a higher roughness. The broadness difference of the Laue fringes can be explained by slight differences in the sample film thickness. The 99nm sample of the low deposition rate series will be discussed below.

The cut through profile in figure 4.35 in position one of the AFM micrograph (figure 4.34) shows the appearance of only 4 partial layers, confirming pronounced layer growth.

With the *Stochfit* software no accurate fits could be achieved, so in the following only the fit with *X'Pert Reflectivity* is shown. For the fit a model with the 38 times copy of one layer (figure 4.36), again for a low number of parameters, together with the substrate, shows the best fit plotted in

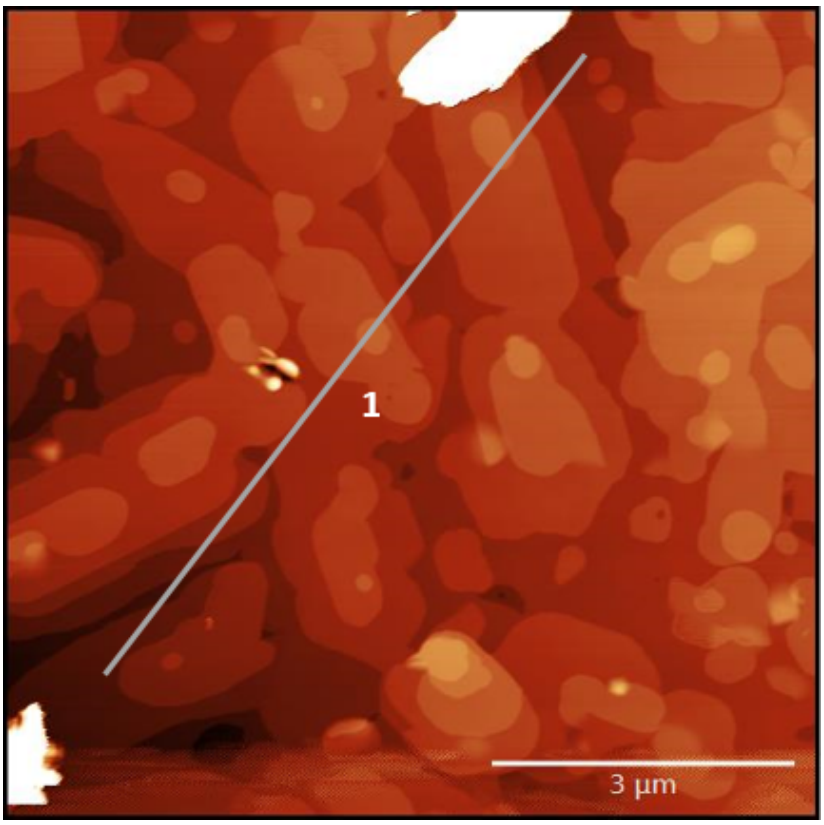

Figure 4.34: Atomic force microscopy micrograph of the low deposition rate sample with a nominal thickness of 99nm. The white line is the place of the cut through below

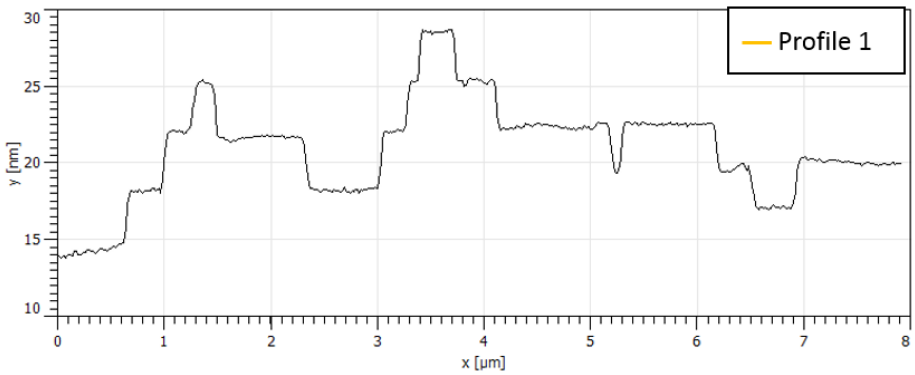

Figure 4.35: Height profile of the cut through the atomic force microscopy micrograph

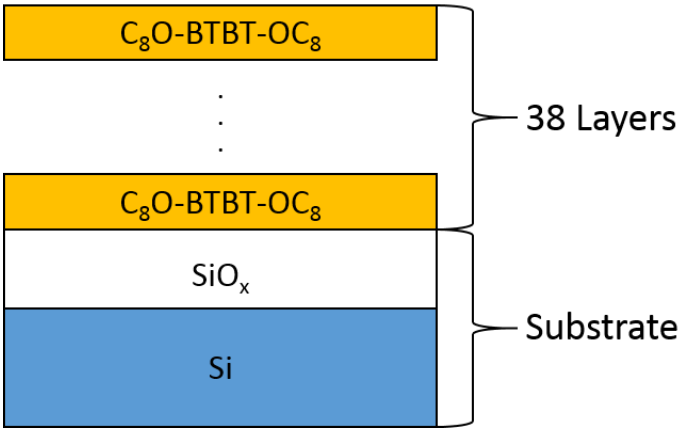

Figure 4.36: Schematic layer model for the *X'Pert reflectivity* fit

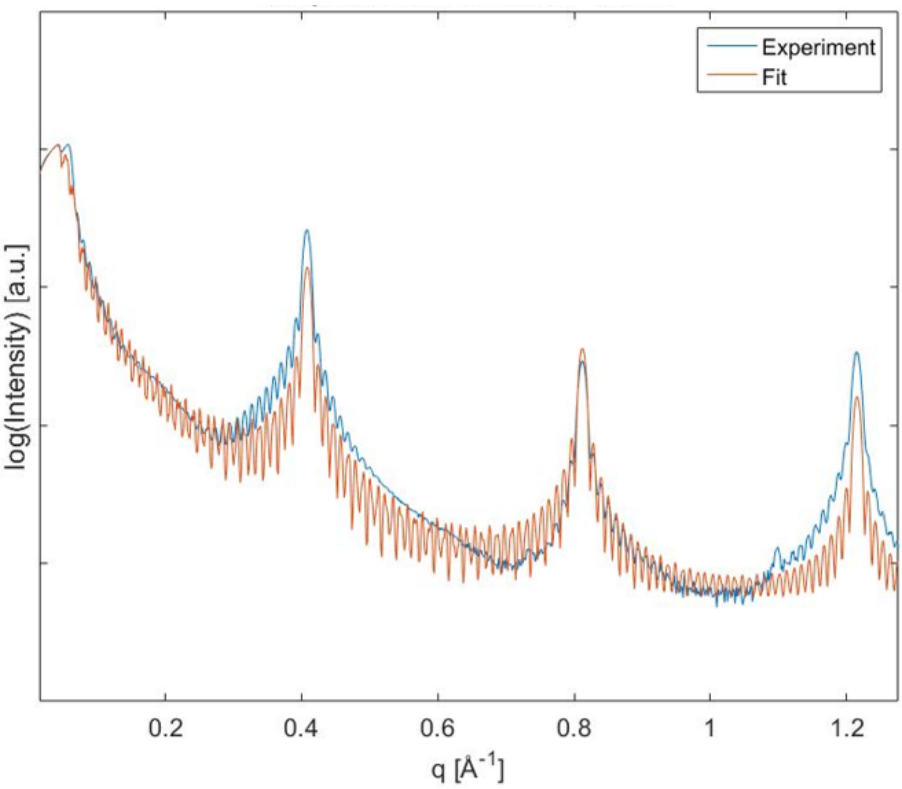

Figure 4.37: *X'Pert Reflectivity* fit of the X-ray reflectivity measurements of the low deposition rate sample with a nominal thickness of 99nm

Table 4.7: Result of the *X'Pert Reflectivity* fit for the low deposition rate sample with a nominal thickness of 99nm
ρ_e [nm^{-3}] ... electron density
d [nm] ... thickness
Cov [%] ... coverage (for the calculation see equation 4.5)

Layer	ρ_e [nm^{-3}]	d [nm]	Roughness [nm]	Cov [%]
oBTBT	324	3.09	1.20	86
SiO_2	618	175	1.98	-

figure 4.37. With the thickness and coverage values of table 4.7 the nominal thickness can be calculated.

$$d_{n,XR} = 38 \cdot d \cdot Cov = 102nm \tag{4.10}$$

The result is very similar to the expected value (table 3.1).

5 Conclusion

Due to a very weak signal GIXD delivers only suitable results for samples with a nominal thickness higher then 13nm. All measured samples show the presence of a surface induced phase illustrated in table 4.1, independent on deposition conditions, for samples up to a nominal thickness of about 100nm prepared by physical vapor deposition. This means that this film preparation as well as spin coating is far from the thermodynamical equilibrium.

AFM pictures show heating the substrate to about 75° increases the domains size of sub-monolayers and multilayers. Sputtering the sample, as well as a high deposition rate has an effect on the diffusion process of sub-monolayers resulting in a different island size. The coverage, directly measured with the AFM and the one calculated via the electron density of the XRR fit, could be compared. Especially for samples with higher coverage the AFM measured coverage is bigger than the one of the fit. The cut through multilayer AFM profiles, thicker than 13nm, reveals pronounced layer by layer growth of C_8O-BTBT-OC_8 with maximal 4 partial layers. Especially the first layer immediately gets filled. The fitting software *Stochfit* is a very simple program and useful for sub-monolayers up to a few monolayers. It calculates an normalized electron density profile. Starting with a nominal thickness of 5nm or 1.6 monolayers also *X'Pert Reflectivity* delivers comparable results with layer thickness, density and roughness. This software is especially suitable for thicker multilayers.

List of Figures

List of Tables

Bibliography

[1] C. Ruzié, J. Karpinska, A. Laurent, L. Sanguinet, S. Hunter, T. D. Anthopoulos, V. Lemaur, J. Cornil, A. R. Kennedy, O. Fenwick, P. Samorì, G. Schweicher, B. Chattopadhyay, and Y. H. Geerts, "Design, synthesis, chemical stability, packing, cyclic voltammetry, ionisation potential, and charge transport of [1]benzothieno[3,2-b][1]benzothiophene derivatives," *J. Mater. Chem. C*, May 2016.

[2] F. Dinelli, M. Murgia, P. Levy, M. Cavallini, F. Biscarini, and D. M. de Leeuw, "Spatially Correlated Charge Transport in Organic Thin Film Transistors," *Phys. Rev. Lett.*, vol. 92, p. 116802, Mar. 2004.

[3] V. Coropceanu, J. Cornil, D. A. da Silva Filho, Y. Olivier, R. Silbey, and J.-L. Brédas, "Charge Transport in Organic Semiconductors," *Chem. Rev.*, vol. 107, pp. 926–952, Apr. 2007.

[4] M. Mas-Torrent and C. Rovira, "Role of Molecular Order and Solid-State Structure in Organic Field-Effect Transistors," *Chem. Rev.*, vol. 111, pp. 4833–4856, Aug. 2011.

[5] G. Schweicher, Y. Olivier, V. Lemaur, and Y. H. Geerts, "What Currently Limits Charge Carrier Mobility in Crystals of Molecular Semiconductors?," *Isr. J. Chem.*, vol. 54, pp. 595–620, June 2014.

[6] C. Wang, H. Dong, W. Hu, Y. Liu, and D. Zhu, "Semiconducting π -Conjugated Systems in Field-Effect Transistors: A Material Odyssey of Organic Electronics," *Chem. Rev.*, vol. 112, pp. 2208–2267, Apr. 2012.

[7] I. P. M. Bouchoms, W. A. Schoonveld, J. Vrijmoeth, and T. M. Klapwijk, "Morphology identification of the thin film phases of vacuum evaporated pentacene on SIO2 substrates," *Synthetic Metals*, vol. 104, pp. 175–178, July 1999.

[8] C. C. Mattheus, A. B. Dros, J. Baas, G. T. Oostergetel, A. Meetsma, J. L. de Boer, and T. T. M. Palstra, "Identification of polymorphs of pentacene," *Synthetic Metals*, vol. 138, pp. 475–481, July 2003.

[9] B. Wedl, R. Resel, G. Leising, B. Kunert, I. Salzmann, M. Oehzelt, N. Koch, A. Vollmer, S. Duhm, O. Werzer, G. Gbabode, M. Sferrazza, and Y. H. Geerts, "Crystallisation kinetics in thin films of dihexyl-terthiophene: the appearance of polymorphic phases," *RSC Adv.*, vol. 2, pp. 4404–4414, May 2012.

[10] O. Werzer, N. Boucher, J. P. de Silva, G. Gbabode, Y. H. Geerts, O. Konovalov, A. Moser, J. Novak, R. Resel, and M. Sferrazza, "Interface Induced Crystal Structures of Dioctyl-Terthiophene Thin Films," *Langmuir*, vol. 28, pp. 8530–8536, June 2012.

[11] A. Burger and R. Ramberger, "On the polymorphism of pharmaceuticals and other molecular crystals. II," *Mikrochim Acta*, vol. 72, pp. 273–316, May 1979.

[12] R. G. Della Valle, E. Venuti, A. Brillante, and A. Girlando, "Molecular Dynamics Simulations for a Pentacene Monolayer on Amorphous Silica," *ChemPhysChem*, vol. 10, pp. 1783–1788, Aug. 2009.

[13] M. Yoneya, M. Kawasaki, and M. Ando, "Molecular dynamics simulations of pentacene thin films: The effect of surface on polymorph selection," *J. Mater. Chem.*, vol. 20, pp. 10397–10402, Nov. 2010.

[14] A. O. F. Jones, Y. H. Geerts, J. Karpinska, A. R. Kennedy, R. Resel, C. Röthel, C. Ruzié, O. Werzer, and M. Sferrazza, "Substrate-Induced Phase of a [1]Benzothieno[3,2-b]benzothiophene Derivative and Phase Evolution by Aging and Solvent Vapor Annealing," *ACS Appl. Mater. Interfaces*, vol. 7, pp. 1868–1873, 2015.

[15] S. C. B. Mannsfeld, A. Virkar, C. Reese, M. F. Toney, and Z. Bao, "Precise Structure of Pentacene Monolayers on Amorphous Silicon Oxide and Relation to Charge Transport," *Adv. Mater.*, vol. 21, pp. 2294–2298, June 2009.

[16] L. F. Drummy and D. C. Martin, "Thickness-Driven Orthorhombic to Triclinic Phase Transformation in Pentacene Thin Films," *Adv. Mater.*, vol. 17, pp. 903–907, Apr. 2005.

[17] M. Truger, "The Surface Induced Crystal Structure of 6,6'-Dibromoindigo: Origin and Stability," Master's thesis, Graz University of Technology, 2015.

[18] Y. Yuan, G. Giri, A. L. Ayzner, A. P. Zoombelt, S. C. B. Mannsfeld, J. Chen, D. Nordlund, M. F. Toney, J. Huang, and Z. Bao, "Ultra-high mobility transparent organic thin film transistors grown by an off-centre spin-coating method," *Nat Commun*, vol. 5, p. 3005, Jan. 2014.

[19] H. Ebata, T. Izawa, E. Miyazaki, K. Takimiya, M. Ikeda, H. Kuwabara, and T. Yui, "Highly Soluble [1]Benzothieno[3,2-b]benzothiophene (BTBT) Derivatives for High-Performance, Solution-Processed Organic Field-Effect Transistors," *J. Am. Chem. Soc.*, vol. 129, pp. 15732–15733, Dec. 2007.

[20] T. Izawa, E. Miyazaki, and K. Takimiya, "Molecular Ordering of High-Performance Soluble Molecular Semiconductors and Re-evaluation of Their Field-Effect Transistor Characteristics," *Adv. Mater.*, vol. 20, pp. 3388–3392, Sept. 2008.

[21] C. Kittel, *Introduction to Solid State Physics.* Wiley, 8. ed. ed., 2005.

[22] M. Birkholz, *Thin Film Analysis by X-Ray Scattering.* Wiley-VCH, 2006.

[23] http://www.physics.brocku.ca/PPLATO/h-flap/phys7_1.html. Accessed: 2016-04-07.

[24] R. Resel, "X-ray physics," Lecture notes, Graz University of Technology, 2014.

[25] C. Lercher, "Surface Induced Polymorphism of Dioctyl-Terthiophene on Silicon Oxide," Master's thesis, Graz University of Technology, 2013.

[26] K. M. Zimmermann, *Advanced analysis techniques for x-ray reflectivities: Theory and application.* Dissertation, University Dortmund, 2005.

[27] M. Born and E. Wolf, *Principles of Optics.* Pergamon Press, 6. ed. ed., 1993.

[28] S. M. Danauskas, D. Li, M. Meron, B. Lin, and K. Y. C. Lee, "Stochastic fitting of specular X-ray reflectivity data using *StochFit*," *Journal of Applied Crystallography*, vol. 41, pp. 1187–1193, Dec. 2008.

[29] A. Erko, I. Packe, C. Hellwig, M. Fieber-Erdmann, O. Pawlizki, M. Veldkamp, and W. Gudat, "KMC-2: the new x-ray beamline at BESSY II," in *AIP Conference Proceedings*, vol. 521, pp. 415–418, AIP Publishing, June 2000.

[30] N. A. Geisse, "AFM and combined optical techniques," vol. 12, pp. 40–45, 2009.

[31] D. Nečas and P. Klapetek, "Gwyddion: an open-source software for SPM data analysis," *centr.eur.j.phys.*, vol. 10, pp. 181–188, Feb. 2012.

[32] O. Werzer, B. Stadlober, A. Haase, H.-G. Flesch, and R. Resel, "Evaluation of organic sub-monolayers by X-ray based measurements under gracing incident conditions," *The European Physical Journal - Applied Physics*, vol. 46, p. 20403, May 2009.

[33] R. Ruiz, D. Choudhary, B. Nickel, T. Toccoli, K.-C. Chang, A. C. Mayer, P. Clancy, J. M. Blakely, R. L. Headrick, S. Iannotta, and G. G. Malliaras, "Pentacene Thin Film Growth," *Chem. Mater.*, vol. 16, pp. 4497–4508, Nov. 2004.

[34] M. Dohr, "Temperature induced effects of dioctyl-benzothieno-benzothiophene thin flms," Master's thesis, Graz University of Technology, 2012.

[35] A. Neuhold, H. Brandner, S. J. Ausserlechner, S. Lorbek, M. Neuschitzer, E. Zojer, C. Teichert, and R. Resel, "X-ray based tools for the investigation of buried interfaces in organic electronic devices," vol. 14, pp. 479–487, 2013.